Electron Vortex Beams: Production and Propagation

Laura Alice Clark

MSc (by research)

University of York

Physics

August 2012

Abstract

Electron vortex beams are electron beams which carry orbital angular momentum. They can be produced within an electron microscope by illuminating an appropriate holographic binary foil mask with a coherent electron beam.

In this work, the design of the holographic masks is investigated and found to be highly adaptable in producing a desired set of electron vortex beams through simple mask alterations. A number of mask parameters have been studied in order to determine what vortex beam properties can be produced experimentally.

The vortices form as the beam propagates beyond the mask, and exist in the far–field. The propagation of the beams has been studied in the near–field of the mask to display the vortex formation process, and studied in the far–field of the mask to predict the behaviour of the beams in the image plane of the electron microscope. This propagation series has been qualitatively compared with experimental data.

Finally, the effects of applying variously shaped apertures on the vortex beams was studied. From the produced simulations it is predicted that non–cylindrically symmetric apertures will cause a splitting of high–order vortex beams into lower orders. The splitting behaviour is dependent on the order of orbital angular momentum, and as such, is expected to be useful as a measurement tool. This is analogous to established behaviour reported in optical vortex beam literature.

Contents

List of Figures

Acknowledgements

I would like to acknowledge the guidance of Prof. Jun Yuan, my supervisor, and the support and encouragement of Prof. Mohamed Babiker. I would also like to thank Dr. Jo Verbeeck, who enabled a month–long research visit to study at EMAT, University of Antwerp, the products of which are combined into this dissertation.

I greatly appreciate the support of Dr. Thirunavukkarasu Gnanavel, who performed the experiments which provided the data for comparison with the theoretical simulations and advised on experimental context. I would also like to thank Richard Aveyard for coding advice, meticulous proof–reading and tea provision, and to thank Sophia Lloyd for discussions of the relevant mathematics.

I am also indebted to Brown's of Heslington for their many sandwiches providing sustenance throughout my studies at the University of York. Last, but in no way least, I thank my parents for their constant support (financial and otherwise!) without which I would not have been able to undertake this opportunity.

Author's declaration

I hereby declare that this dissertation is the result of my own work, except where explicit reference is made to the work of others, and has not been presented in any previous application for a degree at this or any other institution.

Signed:.....

Laura Alice Clark

Chapter 1

Introduction

The field of electron vortex beams is a very exciting area of research, as it is not yet five years old. It calls upon a broad range of physics – from quantum mechanics [3, 4] and nanophysics [5], to optics and materials science [6]. It is also a field in which many fundamentals are still unknown – each new piece of research really is a new discovery at this stage.

Several subsections of this work have been presented at conferences or published in the peer-reviewed literature. These sections are highlighted at the relevant point in this dissertation.

We begin by discussing the field of research and defining some of the key terms. This enables us to follow with a historical overview, describing the most important discoveries leading to the development of the vortex beam. From here we discuss the development of the electron vortex beam with regards to both experimental and theoretical aspects.

This chapter concludes with a discussion of the motivations for the research – being of fundamental interest, and some technological application – and the aims and objectives of this work. We then lay out the structure of the remainder of the dissertation to guide the reader.

1.1 Vortex beams

Before we can discuss the literature and the new research carried out so far in the field, it seems prudent to begin with a brief introduction to the field.

Vortices can be a property of many media, and can be observed in varied disciplines of study; from fluid dynamics and atmospheric physics, to condensed matter physics or radio communications. The vortex beam (as a particular case of vortex behaviour) also exists in several fields. Firstly, we will discuss the general case, followed by a focussed discussion of electron vortex beams.

A vortex beam is a beam with helical wavefronts, twisting around the beam axis. This feature leads to a number of unusual properties.

The wavefronts have a structure similar to that of fusilli pasta, all meeting at the beam axis. As each wavefront represents points of constant phase, the meeting of different wavefronts means the phase is indeterminate at the central point. This is described as a phase singularity, and exists along the length of a vortex beam axis.

Figure 1.1: Fusilli, representing the wavefront structure of an $l = 3$ vortex beam. Figure courtesy of [1].

There is an intensity zero along this singularity due to the indeterminate phase. This results in vortex beams having a doughnut–shaped intensity profile (a set of concentric rings is also a possibility). The central intensity zero is not diminished over propagation which distinguishes it from non–vortex, ring–shaped beams. See figure 1.2 for an illustration of these features.

It is well known that both electromagnetic radiation and matter carry momentum. The direction of the momentum is normal to the wavefront, and hence in vortex beams we have an orbital angular momentum (OAM).

OAM is distinct from the more familiar spin angular momentum (SAM). OAM is usually an extrinsic angular momentum, as it depends on the gross motion of the particle [7].

This is in contrast to the intrinsic nature of of SAM. The OAM is quantized and takes values of $\pm l\hbar$ per particle, where l is an integer. There is no theoretical upper bound. This is in contrast with the $\pm\hbar$ limit of SAM of a photon, and $\pm\frac{1}{2}\hbar$ limit of SAM for an electron.

In OAM beam wavefunctions, l is the azimuthal mode index. l also describes the number of times within a wavelength the wavefront wraps around the beam axis and thus can be referred to as the winding number of the beam. Vortex beams require a term of the form $e^{\imath l\phi}$ (where ϕ is the azimuthal coordinate, and l is an integer) to describe this.

1.2 Historical overview of vortex beam research

To build towards the clearest understanding of the vortex beam, we will first review the key papers and research in the development of vortex beams. The first vortex beams were all beams of electromagnetic radiation, and when considering the momentum properties of photons, we must note that this property was first predicted following from Maxwell's electromagnetism [8].

The photon spin property was first applied by Poynting in 1909 [9]. In his paper, Poynting theorised that a circularly polarised beam of light should carry an angular momentum, and that this angular momentum should be able to be transferred to an appropriate polarising medium. He also derived the angular momentum transfer rate, which, when quantised shows circularly polarised photons carry $\pm\hbar$ units of angular

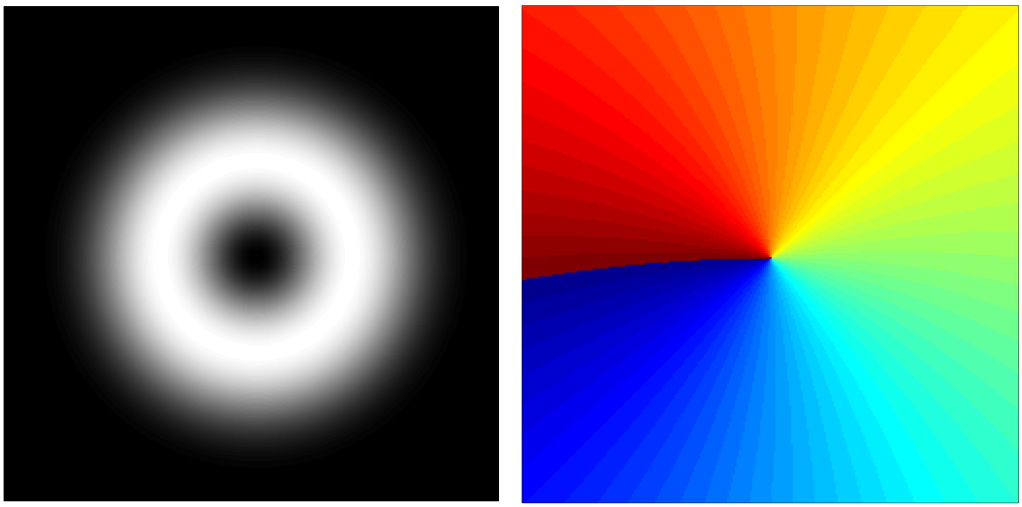

(a) Intensity pattern of a typical vortex beam, where the central minimum is clearly visible (arb. units). White= 1, black= 0

(b) Phase variation pattern of a singly twisting vortex beam. Red represents a phase of 0 and blue represents 2π

Figure 1.2: The defining features of a vortex beam

momentum [10]. This is SAM.

Poynting's hypothesis was experimentally verified by Beth in 1936 [11], with an elegant experimental setup to overcome Poynting's pessimistic expectations:

> My present experience of light forces does not give me much hope that the effect could be detected (Poynting 1909 [9])

The next research of direct relevance to the vortex beam field, is the seminal 1974 paper by Nye and Berry, entitled "Dislocations in wave trains". This was prompted by unexpected observations in radio waves reflected from the rough surface of the Antarctic ice–sheet. The reflected waves exhibited jumps in phase, which were categorizeed using the screw–type and edge–type nomenclature of crystallographic dislocations. It was noted that the phase discontinuities always coincided with intensity minima.

It is these screw dislocations and their associated intensity mimima which were recognised as having vortex behaviour (of similar form to those in fluid mechanics).

Soon after this, the first beams considered to have fully helical wavefronts were produced [12], although many of the key features were not yet fully realised. The beams were made by producing a TEM_{01}^{*} mode with a coherent laser. The various orders of TEM (TransverseElectroMagnetic) modes describe the superposition state of the beam, the TEM_{01}^{*} mode being a particular superposition producing the azimuthal phase variation [13]. The true impact of this was not appreciated until the 1992 paper by Allen *et al.* [14] which is regarded by many to be the fundamental paper, beginning the study of vortex beams as an independent area of research. This theoretical paper considered the existence of Laguerre-Gaussian beams as a superposition of the standard Hermite-Gaussian modes in a laser. They derived that such beams, where $l \neq 0$, would have a well defined OAM, and suggested that this could potentially be used to produce a mechanical torque.

Concurrently to this, the field of optical tweezers was also being developed, with pivotal articles published in 1970 and 1986 by Ashkin *et al.* [15, 16]. Optical tweezers

use the gradient forces in a focussed laser beam to trap and manipulate micron sized particles. They are now routinely used in many areas of biological sciences, for which both the length-scale and the forces involved are well suited. For an overview of optical tweezers, see the review articles [17, 18].

The methodology of experimental optical tweezers and the suggestions of Allen *et al.* were combined to produce a new tool, now named the optical screwdriver which is capable of applying a torque to systems at, and below, the micron scale [14, 19].

Following the 1992 paper, other papers on vortex beams swiftly followed. Vortex beams were considered quantum mechanically [20], their interactions with other vortices, and with molecules were studied [21, 22] and many more complex experimental configurations were developed [23, 24, 25]. By the turn of the century, there was a broad range of studies on many aspects of optical vortex beams, and the subject became an established field of research prompting a comprehensive review article [26] and a journal special issue [27]. Twenty years from the first vortex beam publication, the field has matured occassioning the publication of a new book, edited by Andrews and Babiker [28].

1.3 Electron vortex beam literature review

By the turn of the millenium, the physics and applications of vortex beams were well established, and had been employed in a broad range of fields, as noted in contemporary reviews [29]. Vortices had been produced across a broad range of the electromagnetic spectrum [29].

In 2007, a truly insightful paper by Bliokh *et al.* [3] reported that the vortex properties could also be produced in de Broglie particle waves (a realisation also alluded to in the conclusion of Nye and Berry's paper [30]). It was proven that the time-dependent Schrödinger equation allows for electron beams with a Laguerre-Gaussian structure, in which the electron beam probability current would follow a helical path around the beam axis. Bliokh *et al.* also suggested two possible methods of electron vortex (EV) production: the spiral phase plate, and the holographic mask. As shall be discussed below, both have since been sucessfully demonstrated.

The first experimental EV paper utilised the spiral phase plate technique, in which a lens is constructed with its thickness increasing with azimuthal angle [31]. Such lenses deform planar wavefronts into a continuous helix to introduce OAM. This is an established method in the optical vortex (OV) regime. To achieve this correctly, the maximum phase delay must be adjacent to the minumum phase delay, and their difference must be an integer multiple of 2π. This requires a very precise step height which places very high demands on the manufacturing. The demands of the smaller EV scale exceeds current manufacturing capabilities.

The spiral phase plates have a higher refractive index than the surrounding medium. The wavefront incident on such structures is retarded by an amount proportional to the local thickness of the plate. This results in an outgoing beam with a helical wavefront, having acquired an OAM. The wavefront structure is shown schematically in figure 1.3.

To create a continuous spiral wavefront, the step-height must be designed as a function

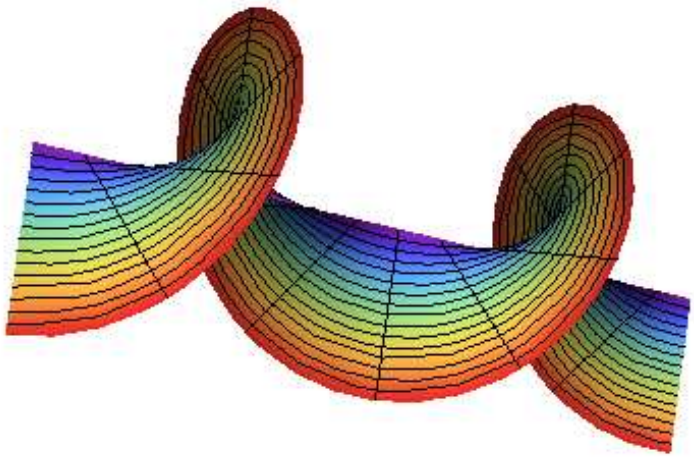

Figure 1.3: A representation of an $l = 1$ beam wavefront, seen twisting around its central axis. Figure courtesy of [2]

of both intended wavelength and refractive index, according to:

$$s = (n - 1)\lambda l \tag{1.1}$$

where s is the step height, l the winding number and n the refractive index of the phase plate [10]. This is assumed to be in air or in vacuum. This structure requirement leads to experimental challenge. Spiral phase plates can be produced for optical wavelengths and longer, and have found commercial application [32].

Creation of spiral phase plates on the $\lambda = 10^{-12}m$ scale however, is more challenging. Uchida *et al.* instead searched through a sample of graphite for a spiral-type stacking of layers, which could constitute a spiral staircase approximation to the phase plate [31]. The spiral staircase region found by Uchida *et al.* was able to produce an electron vortex with $l = 1$. The vortex beam was produced by illuminating the spiral–stacked region with a planar electron wave in a transmission electron microscope. The phase structure was verified using an interference method. The incoming beam was split in two, one half passed through the phase plate, the other half did not. These two beams were recombined at the imaging screen to produce an interference pattern. The pattern produced showed a two–pronged fork–type defect, the mark of an $l = 1$ screw–type defect in a beam.

While this clearly demonstrated a proof of concept, there are limitations to this method. It is not consistently repeatable, due to the difficulties in producing the phase plate, and it will depend on the precise nature of the sample selected. This method is also limited to low orders of OAM, as the thicker phase plate required would reduce the intensity of the beam able to pass through. High intensity beams would increase beam damage to the sample. However, it is a simple analogue of some early OV experimental cases [33] and an elegant method of phase manipulation of an electron beam by applying elementary optics.

A simpler method for creating EVs lay in Bliokh *et al.*'s other suggested technique: the holographic mask, this was demonstrated by Verbeeck *et al.* in 2010 [6]. The holographic

mask technique produces EVs using a forked diffraction grating – the fork pattern being the result of a mathematically produced interference pattern between the desired OAM beam and a planar reference wave. The inteference pattern is binarised to create the desired mask. This production technique and the resultant beams are the subject of this dissertation.

The mask produces a set of output beams: a central zero–order beam carrying no OAM, and many subsidiary beams to the left and right with increasing orders of $\pm|l|$. The mask can be produced with a typical focussed–ion–beam machine, and the beams produced with this technique are, by design, of integer order [6]. The repeatability and adaptability of this technique was demonstrated by the swiftly following paper by McMorran *et al.*, in which EVs with an OAM of up to $l = 100$ were produced.

These early experimental results have been neatly collated and explained in more detail in an article by Schattschneider *et al.* [34], which additionally considered simple aberrations and the effect of imperfectly coherent electron sources. It was found that small aberrations did not affect the topological character of the beam, allowing the vortex to propagate fully, however, the source coherence was found to be of key importance, with small levels of incoherency able to destroy the vortex state. Source coherence is measured by its convergence angle. Schattschneider *et al.* suggest maximum source angular width of $\leq 0.01\mu rad$ with a $25\mu m$ radius mask. The simple analytical model set out in the paper allowed the first quantitative understanding of EVs and their behaviour.

The papers described thus far laid out the first key steps to understanding EVs, both in theory and experiment. From these, researchers have been able to develop the concepts further to potential applications of EV beams.

The first true application was reported in [6], in which EVs were incorporated into the electron energy–loss spectroscopy (EELS) analysis technique. This allowed for a study of the magnetic response of a sample on a previously unreachable scale, as the EV carries with it a magnetic moment [34]. Non–vortex EELS, in contrast, studies the electric response of a sample. The theory of vortex–EELS has since been studied in depth [35].

Whilst vortex–EELS offers a significant improvement in magnetic measurement resolution, it is noted in [10] that compared to an equivalent $l = 0$ beam, the corresponding vortex beam will have a larger diameter (and the diameter will increase approximately linearly with l [36]). Thus achieving the goal of atomic resolution vortex–EELS will be more difficult than non–vortex EELS.

Idrobo and Pennycook [37] theorised that atomic resolution vortex beams are not possible in current electron microscopes. They suggested that either a much higher voltage would be required (of the order of 2MV, compared to the typical 200kV) or that the electron beam be changed to an ion source in order to enable sufficiently small EVs.

Following soon, Ångstrom scale EVs were produced within a TEM [38, 34]. The smallest of these had diameters of 1.2Å, but with the central minima reduced due to the finite source size [38].

Subsequently, the next step towards implementing vortex-EELS was to allow use within a scanning transmission electron microscope (STEM) which rasters across a whole sample. For this, only one vortex must be in focus on the sample at a time. This was achieved [39] by altering the structure of the holographic mask by changing the reference wave from planar to spherical. This focusses the orders along the z-axis, rather than

across the xy-plane. Echoing the earlier developments, this paper was swiftly followed by another, demonstrating the application of this technique to very high order beams [36].

In addition to the application–targeted developments, there have been further studies into the fundamentals of EV interactions with other systems. The simplest case studied how OAM can be transferred from an EV to atomic electrons [4]. Theoretical studies have also found EVs as a solution of the full Dirac equation, accounting for both relativisitic effects and spin [40]. This work made the interesting prediction of a spin-dependent radial distribution of the vortex beam, which is expected to be experimentally observable [40].

There is also an analysis of EV behaviour propagating through a crystal sample [41]. This reveals a number of effects which will be key in interpreting future experimental results, including local non-conservation of vorticity, and channelling of the vortex centre down the crystal columns, which predicts a strongly position–dependent behaviour.

There are also studies of EV–EV interactions, EV–plane wave interactions and a discussion of the potentially vortex–entangled resultant states [42, 43, 44].

The field of EVs seems ready to expand rapidly, with many papers suggesting future uses for EVs [6, 35, 4], which have not yet been investigated, and an established sister field of optical vortices from which we can use many ideas for inspiration [29].

1.4 Experimental context: electron microscopy

The study of electron vortex beams is interesting from a theoretical physics viewpoint, but also of interest within an experimental situation. While, hopefully, the theoretical interest will justify itself, to demonstrate the experimental potential of electron vortex beams, a brief overview of electron microscopy follows to explain the environment currently best situated to employ this new physics.

To create stable electron vortex beams, we require coherent monochromatic electron waves. These are readily available within an electron microscope.

Modern electron microscopes typically operate at accelerating voltages between 200-300kV, leading to typical wavelengths of $2 \times 10^{-12}m$ to $2.5 \times 10^{-12}m$ (with relativistic corrections considered). This scale is $1/250000^{th}$ of the wavelength of visible light, and thus electon microscopes enable us to see detail at the atomic scale [45].

It is now possible to routinely create EVs in the electon microscope. Consequently, the vortex interaction behaviour [4] can be applied to existing microscopy techniques [6] to study new fundamental physics. The EV has thus far been employed in the transmission electron microscope (TEM), and in the scanning-TEM (STEM). These both involve different system setups and are designed to enable the study of different properties [45]. The TEM is designed to create diffraction patterns of very thin films by sending electrons through the sample, and recording at a screen below. See figure 1.4 for a schematic of the simplest TEM setup.

The sample is illuminated with a planar wavefront, and the diffraction pattern recorded below with either a photographic film or a CCD screen. The holographic mask used to create the EVs can either be placed in the sample plane, to allow for a study of the vortices themselves, or placed in the condensor aperture, to allow EVs to impinge upon a sample to study their interactions.

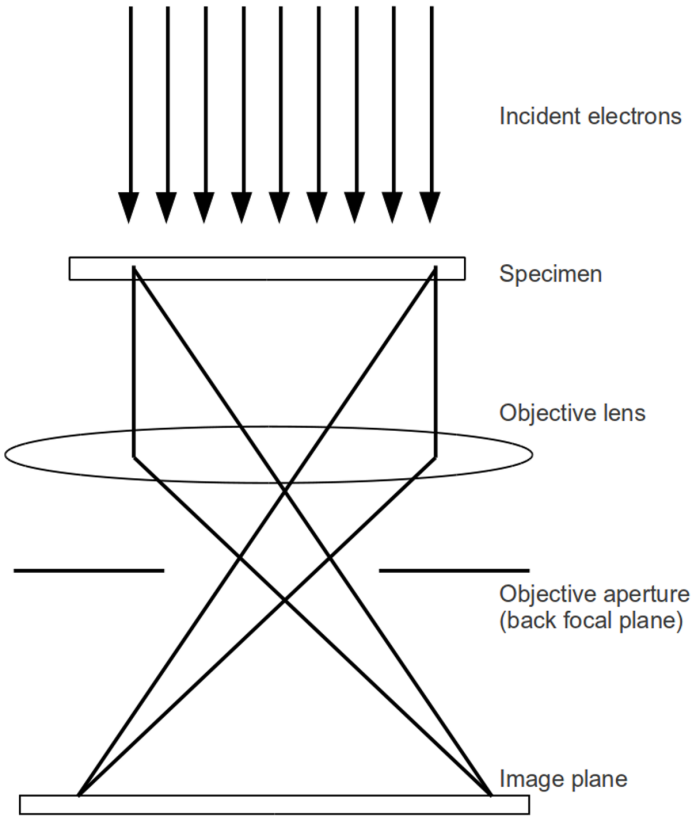

Figure 1.4: Simple schematic diagram of a TEM

In contrast, the STEM illuminates the sample with a focussed probe beam, which is rastered across the sample. This allows for a number of different imaging modes, studying the electrons as a function of their diffraction angle. See figure 1.5 for an example STEM setup.

For a complete overview of the experimental context, the method used to create the holographic masks should also be considered. The technique applied involves cutting a thin foil with a focussed ion beam. The focussed ion beam patterns or cuts the foil sample from a computerised design provided, with a resolution of up to $7nm$. This resolution estimate is an ideal resolution however, and to produce a mask that will truly block electrons where required thicker foil is required. The thicker foil reduces the achievable resolution of the focussed ion beam machine. Additionally, due to the fragility of the foil, and the intricacy of some designs, support bars may also need to be designed into the pattern, to reduce strain related deformities such as stretching or warping of the mask.

1.5 Motivation and objectives

After studying the currently available literature it is noted that there is little research into how the beams propagate both in the near field just behind the holographic mask, and in the far field, where the vortex features are at their most clear. To enable the development of vortex beams for useful technological application, it is crucial that the spatial and temporal evolution of the beams is characterised and shared within the electron

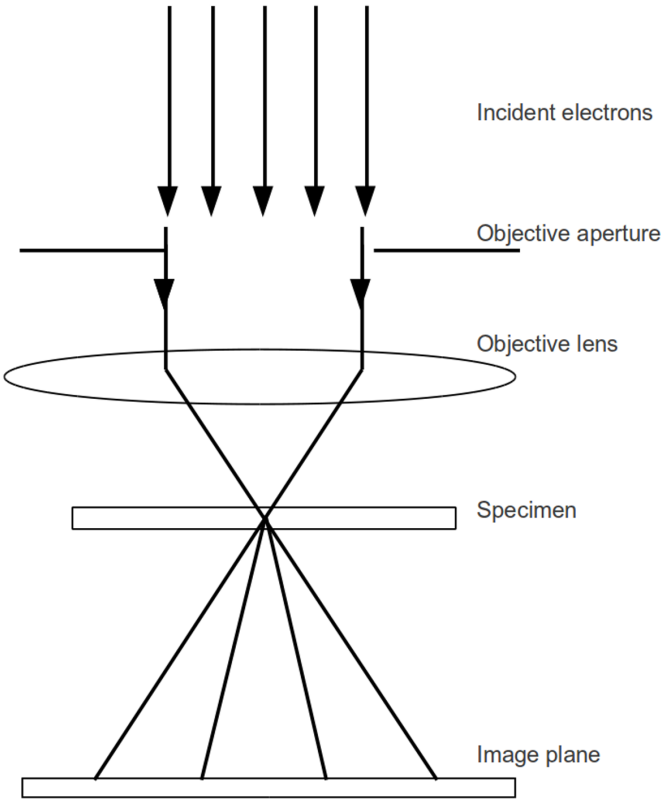

Figure 1.5: Simple schematic diagram of a STEM

microscopy community. It is to this aim that the research described in this dissertation looked into mask designs for the creation of electron vortex beams, with their corresponding efficiencies, and also into the behaviour of the diffraction and propagation of the electron beam post-aperture.

1.6 Structure of this dissertation

This introduction is followed by a review of the methodology and the theory required to develop computational models of electron vortex beams. This includes broader areas of relevant optics theory and techniques, and their specialised application to this purpose.

The dissertation then progresses onto three research chapters detailing the modelling and its results. The first of these is a study into the finer details of holographic masks, and the effect of these variations on the vortex beams produced by them. This includes consideration of radial distribution functions aperture radii and binarisation levels. The application of each of these techniques to different experimental areas is discussed.

These ideas are developed further in the next chapter, wherein we note the effect of the geometric aperture shape on the near-field propagation from behind the holographic mask. Both pure OAM beams and those produced using the holographic mask technique are considered.

The natural counterpart of the near-field study, is the far-field study. In the far-field of the holographic mask, the vortex beams are stabilised, allowing for the study along the lines of classical optics – investigating Rayleigh length, waist diameter and the behaviour

of a variety of beams over a defocus series.

All the features noted above are brought together in the conclusions chapter, as an overview of a well-rounded electron vortex simulation tool. From here we are able to note many future avenues of research, which it is hoped will be able to make a valuable contribution to the rapidly developing field of electron vortex beams.

Chapter 2

Methodology

This chapter will review the purpose of this research and the methods applied in working to fulfil these aims. In order to describe the methods with clarity, the relevant mathematical theories will first be described and their translation into computational methods will be discussed.

2.1 Project aims

Our current work investigates the creation of electron vortex beams through the method of computer–generated holography. This was achieved through the development of a program written initially in Mathematica and then extended and developed using Matlab. The final codes are presented in the appendices. The program produces designs for vortex–inducing holographic masks, predicts their far–field intensity and phase distribution patterns and models their propagation over space.

In addition to the computational and theory work, there is also experimental application to electron vortex beams studied by Dr Thirunavukkarasu Gnanavel [46]. These results are discussed alongside the associated computational results at the appropriate point in chapters 3–5.

We begin this methodology section discussing the structural forms of vortex beams which exist and can be modelled. This is followed by an overview of the required theory to build holographic masks, image the far–field and simulate spatial propagation.

2.2 The structure of OAM beams

There are two common modes of vortex beams, the Laguerre-Gaussian beam and the Bessel beam. The differences between them can be seen in their ring patterns, and their diffractive behaviour.

There are other possible forms of vortex beams, such as the elliptical Mathieu beam [47], however, these beams therefore are not of interest in this study, as use of electron microscopy hardware imposes cylindrical symmetry.

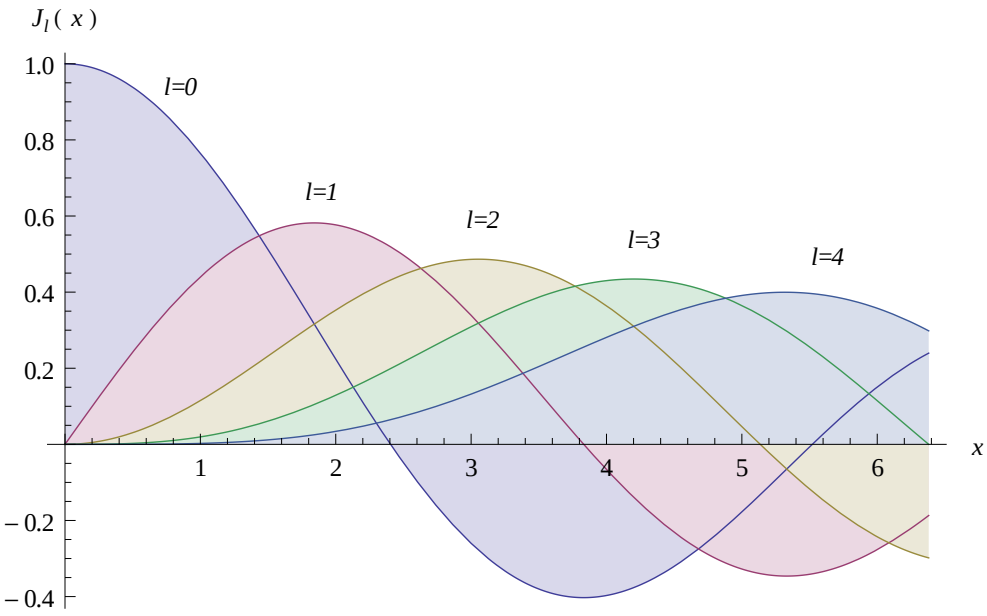

Figure 2.1: The Bessel functions of the first kind, as a function of x, for $l = 1 \ldots 4$

2.2.1 Bessel beams

The ideal Bessel beam has a number of very unusual properties, which make it of interest to study. The Bessel beam wavefunction is a solution of both the paraxial Helmholtz equation and the time-independent Schrödinger equation. Thus we can use it to describe both optical and electron cases. The Bessel beam is described by:

$$\Psi_B \propto J_l(k_r r)\, e^{\pm \imath l \phi}\, e^{\imath k_z z} \tag{2.1}$$

where $J_l(k_r r)$ is the Bessel function of the first kind, of order l, radially dependant on k_r, the radial component of the wavevector, and r, the radial coordinate. ϕ is the azimuthal coordinate, and z is the axial coordinate. k_z is the axial component of the wavevector, such that $k = \sqrt{k_z^2 + k_r^2}$.

We can see that Bessel beams are modulated radially by a Bessel function of the first kind. The Bessel functions are a solution to Bessel's differential equation, and are a function of l and r, where l is an integer and r is the radial distance from the axis of propagation. Figure 2.1 shows the variation of the Bessel function, $J_l(x)$, against x. In this case, $x = k_r r$.

It can be seen that for all orders other than $l = 0$, the Bessel function passes through the origin. In cylindrical coordinates, this point corresponds to the central minimum at the vortex core.

We can note from figure 2.1 that for increasing $|l|$, the positions of the maxima move away from the origin and are reduced. A true Bessel beam has an infinite width [48]. It follows that producing an ideal Bessel beam requires an infinite amount of energy and is thus impossible.

A novel property of an ideal Bessel beam is that it is entirely diffraction free. The propagation term of the Bessel function depends only on the axial position and is inde-

pendent of radial position [48]. In experimentally realisable Bessel beams, this translates to significantly reduced diffraction of the central core, in comparison with an appropriate Gaussian or Laguerre–Gaussian beam [49].

There are several methods to approximate an ideal Bessel beam. Published approximations to Bessel beams include applying a hard-edged aperture, thus forcing a convolution with an Airy disk [50] or applying a Gaussian envelope over the function to force the function to tend to zero at inifinity [51]. The Bessel–Gaussian beams are of particular use in experiment as they can be produced to be highly similar to their theoretical model [51], and are thus a very realistic approximation to the ideal Bessel beam.

Another feature of the ideal Bessel beam is its ability to self-reconstruct. After part of the beam is blocked, the previous pattern will be recreated further along the beam axis [48]. It is not yet exactly clear how this will be of use in EV situations, however, this would be largely dependant on the experimental setup and aims. There is hope for this feature to be of use in the future.

2.2.2 Laguerre–Gaussian beams

Laguerre–Gaussian beams can also be found as a solution of the paraxial Helmholtz equation and the time–independent Schrödinger equation and thus are also an appropriate framework with which to describe OVs and EVs [52].

As suggested from the name, LG beams combine a Gaussian beam envelope with a generalised Laguerre polynomial. The generalised Laguerre polynomial has two indices: the azimuthal index l and the radial index p. Varying the azimuthal index changes the number of radial minima in the in–plane distribution, and it also defines the number of wavefront rotations within one wavelength. Adjusting the radial index varies the number of rings in the beam intensity pattern.

While the Laguerre polynomial affects the in–plane behaviour, the Gaussian terms describe the gross structure of the beam and the behaviour over propagation, and particularly affect the diffraction behaviour. The Laguerre–Gaussian beam is described by a more complex wavefunction than the Bessel beam, and thus we will only discuss the factors of interest.

The entire LG wavefunction is as follows:

$$\Psi_{LG} \propto \frac{1}{\left(1+{}^{z^2}/_{z_R^2}\right)^{1/2}} \left(\frac{r\sqrt{2}}{w^2(z)}\right)^{|l|} \exp\left(\frac{-r^2}{w^2(z)}\right) \exp\left(\frac{\imath k r^2}{2\left(z^2+z_R^2\right)}\right) \exp\left(\imath(2p+|l|+1)\tan^{-1}\left(\frac{z}{z_R}\right)\right) \underbrace{L_p^{|l|}\left(\frac{2r^2}{w^2(z)}\right)}_{(A)} \underbrace{\exp(\imath l\phi)}_{(B)} \quad (2.2)$$

where the first five terms can be ascribed to the Gaussian structure, term (A) is the generalised Laguerre polynomial, where l is the azimuthal index, associated with the vortex term, and p is the radial index where the number of radial maxima appearing in the intensity profile goes as $p+1$. Term (B) is the vortex phase term. $w(z)$ is the waist function, describing the behaviour of the beam over propagation, z_R is the Rayleigh length, the length over which the beam radius increases by $\sqrt{2}$.

The generalised Laguerre polynomial in cylindrical coordinates, has a central zero when $l \neq 0$, where the vortex is found. A central zero is required due to the uncertainty in ϕ which is undefined on axis (ϕ can be defined in Cartesian coordinates as arctan (y/x)).

2.2.3 Comparison of Bessel and Laguerre–Gaussian beams

As the two most commonly discussed types of vortex beams, both Bessel and LG beams warrant consideration for inclusion in this research.

The Bessel beam is described by a simple wavefunction containing the desired features. It has also been studied in a variety of theoretical and experimental OV articles. It is these aspects which make it of interest in this research. It is simple to simulate and model. Pure Bessel theory is simpler to produce than LG theory (and hence its use in papers such as [4, 53]). However, it is not possible to employ Bessel theory directly due to the approximations which must be made. The approximations which must be applied to simulate a realistic Bessel beam rapidly make the results more difficult to interpret, or lose some of the most interesting Bessel–like behaviours of limited diffraction and self–healing. This is discussed further in chapter 3.

The LG beam can be experimentally produced more realistically than the Bessel beam, as a naturally resulting mode of the appropriate laser, or as a modification of the Gaussian distribution of an electron beam. However, the LG beam is more complex to simulate within a propagation model, due to its greater number of interdependent parameters. This can reduce the level of realistic simulations.

As both vortex beam variants have advantages in some areas of study and application, they will both be used in this reseach, as and when most appropriate.

2.3 Holography

The word ‘holography’ is derived from the Greek ‘holos’ meaning ‘whole’, as holography is a technique which captures both the phase and amplitude information of a wavefront [54]. This differentiates it from photography, which only records intensity information. This idea was conceived in 1949 by Gabor, and for this he was awarded the 1971 Nobel prize in physics [55].

The concept of holography revolves around the recording of an interference pattern, between the wave to be reproduced and a reference wave of known form. The recorded interference pattern is referred to as the hologram. If this hologram is illuminated with a beam of the same form as the reference wave, several waveforms are output from the hologram. The most important term of the output waveforms is a reconstruction of the original object wave.

This process was vastly improved in 1962 by Leith and Upatnieks, with the development of off–axis holography [56]. Their technique allows a spatial separation of the output terms, enabling a much clearer observation of the reconstructed object wavefront. The first successful application of holography to electron beams occurred in 1968 [57], following improvements in electron beam coherence [57].

The sub-field of holography which has been applied in this dissertation is called computer generated holography (CGH). In CGH, the interference pattern is a virtual object,

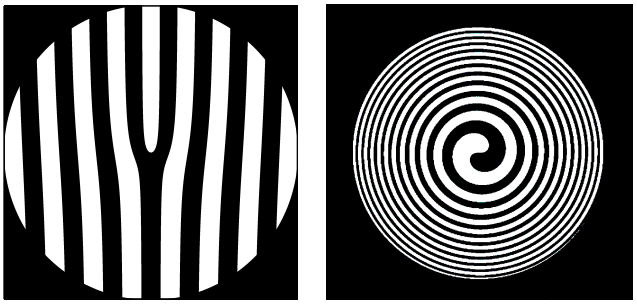

(a) Example of a TEM mask (b) Example of a STEM mask. Figure used from [39]

Figure 2.2: Typical holographic masks for production of electron vortex beams. Both have an arbitrary radius, depending on microscope settings.

only exisiting in a computer program. When this hologram is printed on an appropriate medium and illuminated, the resulting object wave is constructed, appearing in the far-field of the hologram.

The pattern of the hologram would be a grayscale image, ranging from fully opaque to fully transparent. In the optical vortex regime, this can be produced on photographic film. However, there is an alternative to this technique which is simpler to produce in the OV case, and has also been shown to be effective in the EV case. This is the binarised hologram, where regions of greater than fifty percent opacity are rescaled to be fully opaque, and all other areas are set to be entirely transparent, resulting in a pattern resembling a typical diffraction grating. Binarised holograms have been used experimentally with both planar and spherical reference waves for electron vortex beams and optical vortex beams [6, 39, 58, 33]. It is due to this proven experimental viability and interest that this technique will be investigated and developed through this research.

2.3.1 Design of the holographic masks

In the design process it is important to consider the regime in which the mask is used. In the TEM, the mask is illuminated with planar wavefronts, so the appropriate mask is designed with a planar reference wave. In the STEM, a focussed beam is incident on the mask so a spherical reference wave should be used. The object wave to be simulated in the computer program is to be an OAM wavefunction with an $e^{\imath l\phi}$ term. Both the wavefunctions are simulated in the program as complex–valued arrays, where the square of the modulus represents the intensity impinging upon a given point, while the argument describes the phase of the wavefront at that point. The interference pattern is modelled by adding the two arrays together as it is a linear process. The intensity pattern is found by modulus–squaring the interference pattern. This also means all the values are purely real and no longer complex. The intensity pattern is then binarised, following the binarisation process as described above. At this stage, an aperture is also added to the design, usually a centred circle to mimic the symmetries of the system. Typical examples of the resultant masks are shown in figure 2.2

To produce the final holographic mask as required for experiment, the design is cut into a thin foil using a focussed ion beam.

2.4 Fourier transforms as a result of lenses or apertures

The method used within this research to image the far–field of the holographic masks is the two–dimensional discrete Fourier transform. The effect of a lens or an aperture producing a diffraction pattern from an input signal can be mathematically described by a two–dimensional Fourier transform. This can be explained through simple diffraction theory.

The wavefront just after an aperture can be considered as a complex superposition of planar wavefronts propagating with different directions and intensities. The direction of each of these plane waves is defined by its angle from the beam axis, this is the direction of the plane wave's wavevector, $\mathbf{k}$.

The wavevector is also inversely proportional to the wavelength. Thus, the wavevector describes the spatial frequency of the wave. It follows that the far-field of the scatterer is a spatial–frequency sorted representation of the aperture – which is equivalent to a Fourier transform. This is because the Fourier transform describes a function as a weighted superposition of plane waves – the output is a frequency description of the input:

$$F(k_x, k_y) = \iint_{-\infty}^{+\infty} \mathrm{f}(x, y) e^{-2\pi\imath(k_x x + k_y y)} \, \mathrm{d}x\mathrm{d}y \tag{2.3}$$

where $\mathrm{f}(x, y)$ describes the input function in the (x, y) plane and z has been defined as the axis of propagation. k_x and k_y describe the wavevector components in the x and y directions respectively.

The discrete Fourier transform is a method of Fourier transform developed for discrete systems, and as such is ideal for array manipulation programs as in this study. The continuous integral of the Fourier transform is approximated as a finite summation, and computing time required scales as $\mathscr{O}(N^2)$, where N is the number of elements to compute [59]. This method is developed further by application of the fast Fourier transform method, an algorithm that enables the computing time to scale typically as $\mathscr{O}(N \log N)$ and is optimised for arrays with 2^M pixels, where M is an arbirtary integer [59]. There are limits to dependence on the discrete systems, primarily, the sampling rate limits the highest frequency which can be recorded in the array, which is known as the Nyquist frequency [59]. The Nyquist limit is represented by a wavelength of two pixels on a real space array, or wavevectors within the central quadrant of a discrete 2D Fourier transform.

2.5 Fresnel propagation

With the use of Fourier transforms, we are able to image the far–field of a scatterer or aperture. However, to study the propagation of the vortex beam and vortex formation, a technique to model the beam over a series of increasing defocus values is required.

That technique is referred to as Fresnel propagation, as it is built upon the classical optics of Fresnel and Kirchoff [60]. In this research, the propagator method was employed both in the near field behind the aperture and and the far field. This requires a propagator

formation to work in both real and angular space.

We begin with the real space Fresnel propagator, with which we transform our (x, y) plane wavefunction $\psi(x, y, z)$ from the $z = 0$ plane to $(z + \delta z)$:

$$\psi(x, y, z + \delta z) = \exp\left(\frac{\imath\lambda}{4\pi}\delta z \nabla^2_{x,y}\right)\psi(x, y, z) \tag{2.4}$$

This describes propagation in free–space, as described in section 6.4.3 of [59]. Symbols are as previously defined, and $\nabla^2_{x,y}$ is the Laplacian operator in two–dimensions. We employ this equation within a computer program, and thus we rearrange the equation for greater efficiency. Equation 2.4 can equally be written as:

$$\psi(x, y, z + \delta z) = p(x, y, \delta z) \otimes \psi(x, y, z) \tag{2.5}$$

where $\otimes$ represents a convolution [59]. The function $p(x, y, \delta z)$ is referred to as the propagator function and from equation 6.71 of [59] is defined as:

$$p(x, y, \delta z) = \frac{1}{\imath\lambda\delta z}\exp\left(\frac{\imath\pi}{\lambda\delta z}\left(x^2 + y^2\right)\right) \tag{2.6}$$

wherein Huygens' spherical wavefronts are approximated as parabolic, due the Fresnel approximation inherent in equation 2.4. This approximation is valid whilst the diffraction angle is small, and δz is also small, which restricts this model to near–field propagation.

Using this equation for propagation allows use of the convolution theorem [54], which states that:

$$A \otimes B = FT^{-1}[FT(A)FT(B)] \tag{2.7}$$

where A and B are arbitrary functions, FT represents a Fourier transform, and FT^{-1} represents the inverse Fourier transform. This is very fast to compute, as we are able to employ the fast Fourier transform, which is a very efficient algorithm when used on an array size of 2^N pixels [59].

The propagation can be applied successively to the newly propagated wavefront, to model its behaviour over a defocus series (for example, to model the beam over its Rayleigh length, the length over which a beam width increases by $\sqrt{2}$ from the focus).

The propagator term can be converted for use in angular space as [61]:

$$p(\theta_x, \theta_y, \delta z) \propto \exp\left(\frac{\imath\pi}{\lambda}\left(\theta_x^2 + \theta_y^2\right)\delta z\right) \tag{2.8}$$

where (θ_x, θ_y), are the Cartesian coordinates in angular space. These techniques allow for a study of all the space between the aperture and the far field, allowing a study of all points of propagation of the vortex beam. We can consider the far field to have been reached when $z \gg {}^{D^2}/_{\lambda}$ where z is the distance from the aperture and D is the characteristic size of the aperture [62].

2.6 Code structure

The above theory is combined into a code as described in the flow chart seen in figure 2.3. ψ_{OAM} is the desired vortex beam wavefunction and ψ_{ref} is the reference wave chosen.

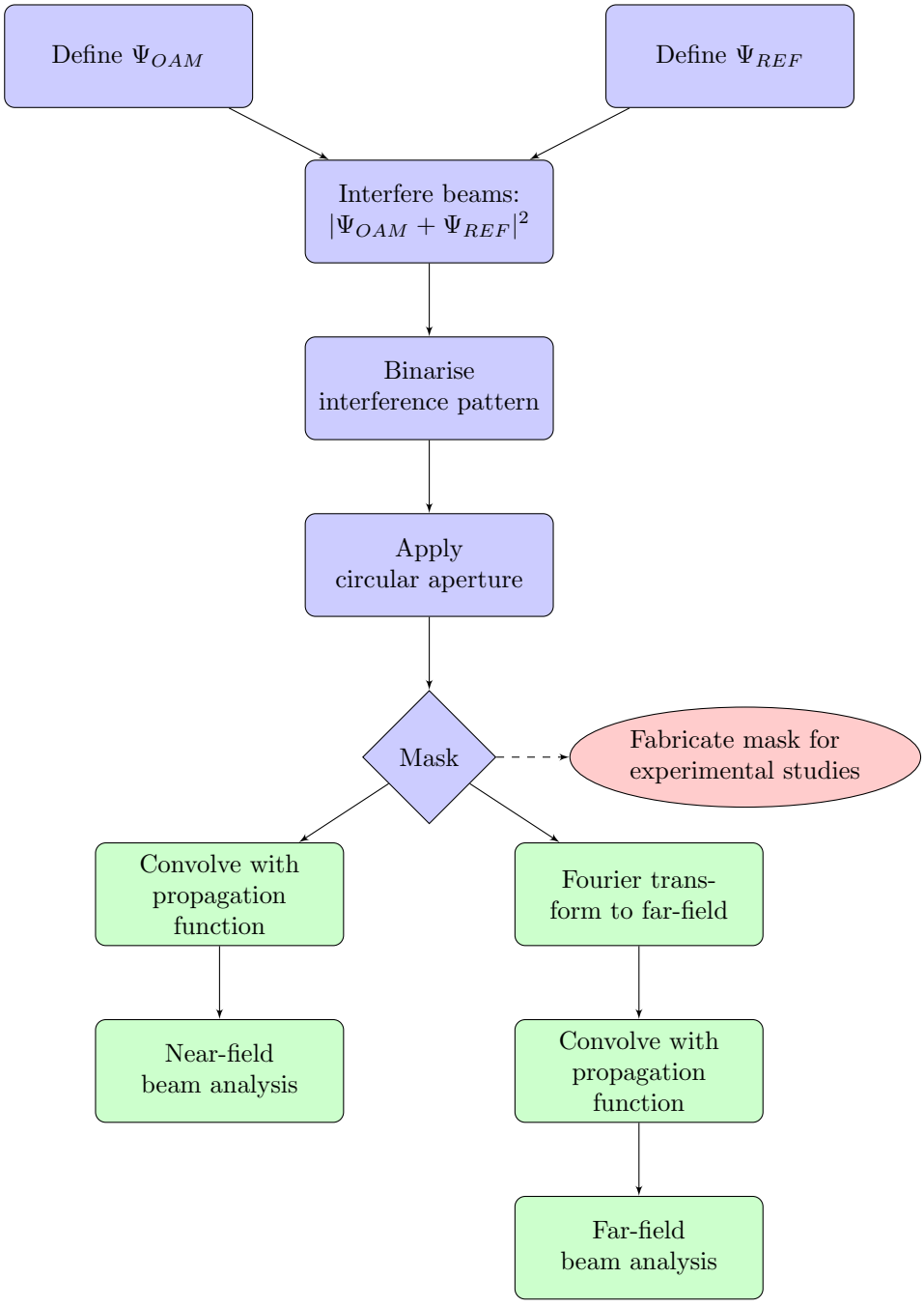

Figure 2.3: Flow chart of primary functions of simulation code

Once the binarised mask is produced, this can be output as an image file to be experimentally produced, or the code can be developed further. The square of the modulus of the Fourier transform represents the far–field intensity of the mask, also referred to as the power spectrum. The argument of the (complex–valued) Fourier transform describes the phase map of the far–field, allowing identification of phase vortices.

The propagation of the system can be studied from two perspectives. To study the propagation of the vortices, equation 2.5 is successively applied over the arrays where we treat the Fourier transform of the mask as $\psi(x, y, z)$. Alternatively, the formation and early evolution of the vortices can be studied instead using the binarised mask array as $\psi(x, y, z)$.

Chapter 3

A study of holographic masks

Holographic masks can be used to produce electron vortex beams [6]. Using CGH to produce the required mask results in a diffraction grating with a fork defect, if a plane wave is used as the reference wave. Alternatively, using a spherical reference wave results in a spiral patterned hologram. In this chapter we focus on the planar reference wave case, as these are appropriate for use in a TEM and have been produced and applied experimentally in York.

It was found by us that the approximations brought into the mask production process such as the aperturing and binarisation can dominate over the small differences between Laguerre–Gaussian and Bessel wavefunctions [63]. We can also note differences between our Laguerre–Gaussian and Bessel far–field results [63, 64] and the far–field results produced in the seminal paper by Verbeeck *et al.*, which applied a different function [6]. The mask differences affect the proportion of the incident beam transmitted to each order of vortex side beam and the internal structure of each side beam. These possibilities are studied and our findings given in section 3.1. The source of both of these effects can be found in the applied radial distribution function – or the mode of vortex beam that has been encoded into the mask.

The holographic masks are further customisable beyond their radial distribution functions. The size of the cut–off aperture in relation to the object wave used will also affect the range of the object wavefunction encoded into the mask. We can also adjust the reference wave spatial frequency in relation to the aperture size, which affects the spacing of the sidebeams in the far–field of the mask. Although this adjustment is a trivial adaptation and application of geometric optics, it is required to find the balance between an experimentally practicable mask, and a mask which will produce sufficiently defined vortex beams.

Combining these effects allows for a fully manipulatable holographic mask which can be designed to produce very specific results. In this chapter, we investigate each of these variables, studying the effects of radial distribution functions, increasing the aperture radius with respect to the object wavefunction and the effect of varying reference wave spatial frequency. Each section will study the design and modelling of the variants, and then consider the effects these changes have on their theoretical far field diffraction patterns.

3.1 Radial distribution function effects

3.1.1 Mask design

This study examines masks resulting from three object wavefunctions, each with differing radial distribution functions. The radial distribution functions studied were the Bessel function, the Laguerre–Gaussian function and a top hat function. These functions were applied in the production of holographic masks as described in section 2.3. Each mask results in a number of vortex beams produced in the far–field. Figure 3.1 shows the masks produced, and figure 3.3 shows the power spectra of the beams due to each of these masks. The central beam has no OAM and thus $l = 0$. The sidebeams have increasing orders of OAM. Changing the radial distribution function applied in the production of the mask is found in this study to alter the relative intensities of each order of side beam.

Here we consider the holographic masks resulting from applying the different radial distribution functions in the interference process and study the effects on the vortex beams in the far–field of the resultant masks. There are several steps required in producing the masks. Here we shall discuss the process as applied to each of the radial distribution functions in turn.

For the top hat function a binary round aperture is applied over the vortex phase term, $e^{il\phi}$, where l is the desired order of OAM. The number of fork tines found in the mask goes as $|l| + 1$. The reference wave is then interfered with the aperture function. This study used a tilted plane wave with a wavenumber in the mask plane of $^{24\pi}/_{R_{max}}$, where R_{max} is the radius of the aperture used. The reference wave is defined in terms of the aperture so that the resulting mask design is independent of mask size.

The modulus squared of the interference pattern is binarised to produce the final mask. In the simple case of the top hat mask, we binarise half–way between the maximum value of 4 and the minimum value of 0. The resultant mask can be seen in figure 3.1a

The production of the Bessel mask requires some additions to the process used in the creation of the top hat mask. The Bessel radial distribution function is infinite in extent and thus needs apodizing at some radius. Here we choose that the cut-off radius should coincide with the first zero of the Bessel function. This limit was chosen as it allows for a standarised radius for all the beams studied. Through altering the encoded radial component of the object wave wavevector (k_r of equation 2.1), the aperture can be scaled to match an arbitrary radius to suit the experimental setup.

The Bessel function is multiplied by the vortex phase term and interfered with a planar reference wave as in the previous case. However, the binarisation process in the Bessel case cannot be applied as simply as above. There are a number of points to consider in the binarisation process. The binarisation must allow the fork feature to remain, as it is this which imparts the OAM to the beam by introducing a discontinuity. The ideal mask must also maximise beam transmittance to minimise the significant reductions in beam intensity which are already inherent in this technique (as discussed in [34]). For experimentally realisable masks, we must also ensure all sections of the mask are connected.

In the Bessel case, binarising at half of the maximum value results in a design in which not all sections are connected, which is of no use for experiment. To avoid this, we binarise slightly below the average intensity of 1.34, binarising at 1 instead, resulting in

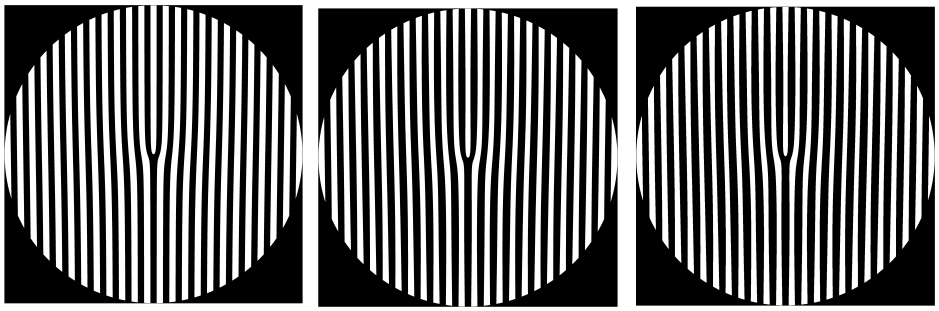

(a) Top hat mask (b) Bessel mask (c) Laguerre–Gaussian mask

Figure 3.1: The holographic masks using the different radial distribution functions. The radius of all masks is $21\mu m$.

a connected forked mask. The value for binarisation was arbitrarily selected from those resulting in suitable masks for fabrication and prolonged application. The resultant mask can be seen in figure 3.1b.

The Laguerre–Gaussian mask is constructed through a similar process to the Bessel mask, however, this radial distribution function introduces a slight complication. The Laguerre–Gaussian radial distribution function uses the generalised Laguerre polynomial, with azimuthal index l, and radial index p, as shown in equation 2.2. For this study, the radial index chosen was $p = 1$. This is the lowest value which produces a ring–shaped minimum to allow for comparison with the Bessel mask, while producing the fewest rings, so as to be most distinct from the many–ringed Bessel function. The Laguerre–Gaussian radial distribution function is then multiplied by the vortex phase term and interfered with the same reference wave as in the previous masks, and binarised at an intensity of 1 as in the Bessel mask. This mask can be seen in figure 3.1c.

The three masks are compared and discussed in section 3.1.2, followed by a discussion of their resultant vortex beams in section 3.1.3. In section 3.1.4 we verify the vorticity of the sidebeams produced in these simulations.

3.1.2 Masks and far field images, produced with different radial distribution functions

Holographic masks have been modelled for the three radial distribution functions as defined above, and shown in figure 3.1. The masks are modelled with a radius of $21\mu m$, to allow comparison with the masks produced in York and employed in the condensor aperture of a double abberation–corrected TEM.

The visible difference between the masks is very small, but can be noted in the curvature of the bars in the mask. The Bessel and Laguerre–Gaussian masks are most similar, with the top hat mask being most clearly different.

There is a maximum difference in aperture coverage area between the masks of 6% between the Laguerre–Gaussian and top hat masks. For computational predictions to be experimentally verified, the masks need to be fabricated at sufficiently high precision. To illustrate the differences between the masks, image subtractions have been performed, the results of which can be seen in figure 3.2.

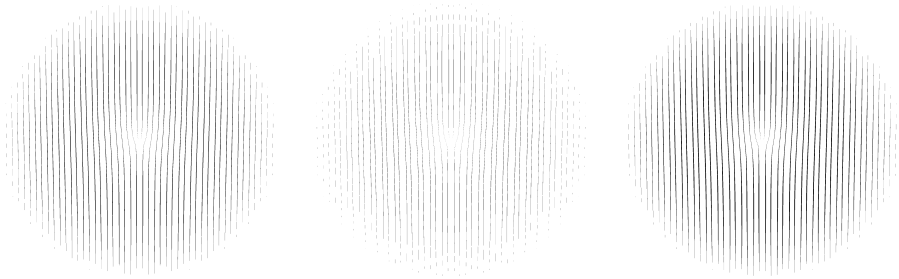

(a) Difference between Bessel and top hat masks

(b) Difference between Laguerre–Gaussian and Bessel masks

(c) Difference between Laguerre–Gaussian and top hat masks

Figure 3.2: A comparison of the differences between the top hat, Bessel and Laguerre–Gaussian holographic masks. Pixels in white are the same in the compared masks, while pixels in black represent the areas of difference.

As we can see, the differences between the subfigures 3.2a–3.2c are very slight, with the Bessel and Laguerre–Gaussian masks being most similar. This is to be expected as the Bessel and Laguerre–Gaussian wavefunctions respectively are more alike than either are to the top hat function.

To consider whether these differences are reproducible in an experimental context, we must compare the scale of these differences with the focussed ion beam (FIB) cutting machine's resolution. The broadest area of difference is found between the Laguerre–Gaussian and the top hat masks, of 0.34% of the mask diameter. In York, masks have been produced with up to $42\mu m$ diameter and to this level of difference would equate to $0.14\mu m$. This is comfortably within the ideal resolution of the FIB, however, most of the regions of difference between the masks are considerably finer and fall below the theoretically possible resolution. The achieveable resolution is coarser than the ideal resolution of the FIB as the effects of the sample material and the machine precision must also be considered, as a thick foil is required. We do not yet have experimental results to compare the far–field intensity patterns of masks produced with the three different radial distribution functions.

3.1.3 Sidebeam intensities

The plots produced in figure 3.3 to image the far field intensity patterns of the holographic masks can be analysed, to quantify the behaviour of the resulting vortex beam intensities. As mentioned above, an important property is the proportion of the incident beam passed into the desired vortex beam order. The top hat mask is based on an even function, and thus has only odd–ordered side beams. This effect has previously been reported by Verbeeck *et al.* [6]. The Laguerre–Gaussian and Bessel masks however, can be expressed as a combination of both odd and even functions and thus will have even– and odd–ordered side beams, with the weightings dependent on the factors of a cosine/sine decomposition. We can verify this through the power spectra figures; figure 3.3b and 3.3c have additional vortex side beams seen at $\pm 4.5\mu rad$, which can be shown to have $l = 2$. These even–ordered side beams do not appear in figure 3.3a.

A study of the side beams was performed, focussing on the first order side beams of the masks, as this represents the order designed into the holographic mask. This was

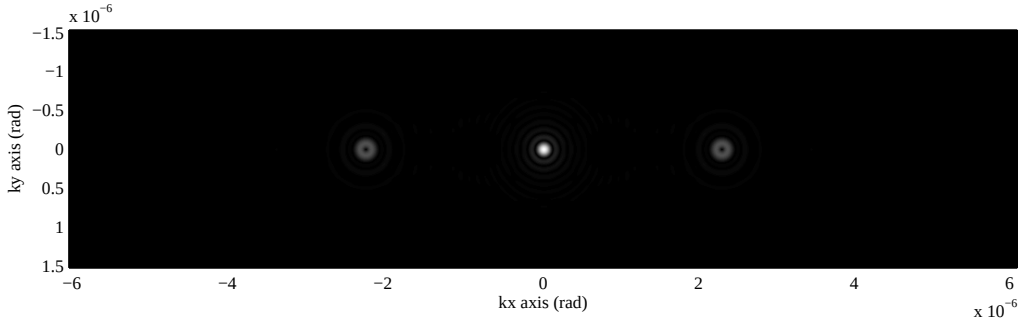

(a) Top hat mask power spectrum

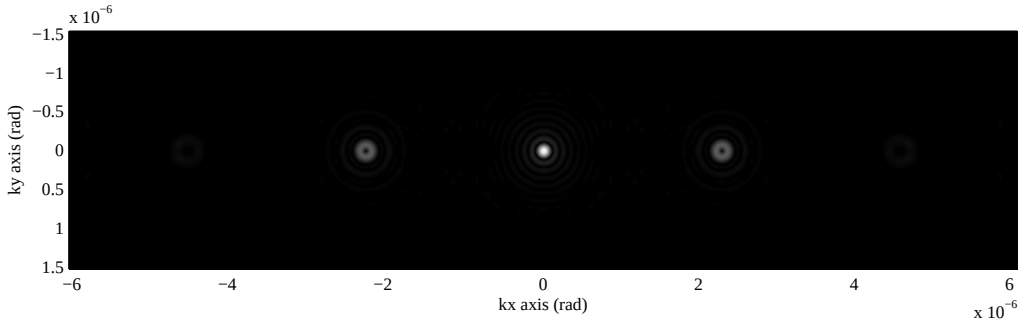

(b) Bessel mask power spectrum

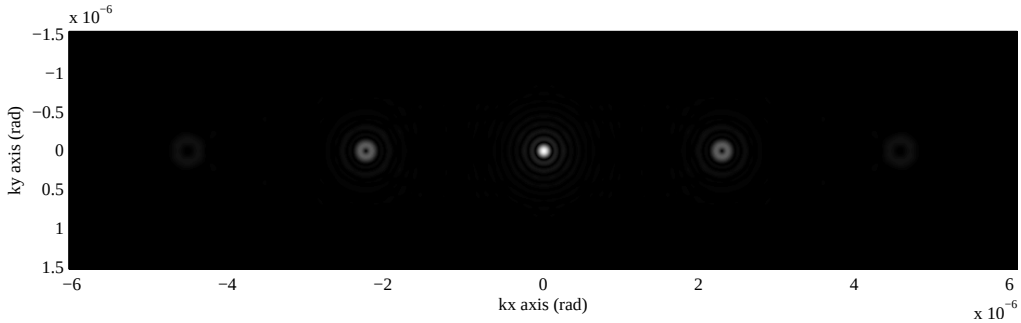

(c) Laguerre–Gaussian mask power spectrum

Figure 3.3: The power spectra from using the different radial distribution functions. Black represents zero intensity, and white represents a maximum intensity.

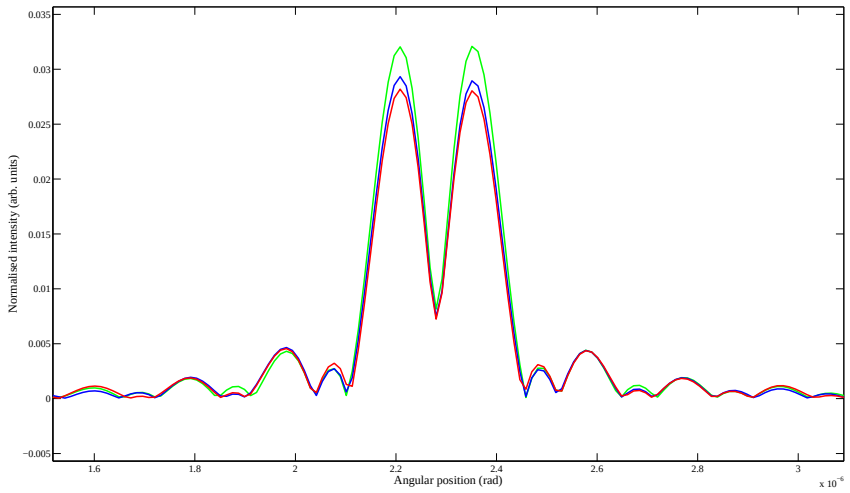

Figure 3.4: Graph of intensity against angular position of the $l = 1$ order side beam produced by the three different holographic masks. Green represents the top hat mask, blue represents the Bessel function mask and red represents the Laguerre–Gaussian function mask

performed by producing an intensity line profile across the middle of the array, slicing across the $l = 1$ order doughnut intensity pattern. This was performed for all three cases, and the result is shown in figure 3.4. We can see from this that the top hat mask produces first order side beams with a $8 - 12\%$ higher peak intensity than the compared Bessel and Laguerre–Gaussian masks. As the top hat mask results in fewer side beams (only producing even–orders) we can expect to see higher intensity in the produced side beams than the intensity of the odd– and even–ordered side beams produced by the Bessel and Laguerre–Gaussian masks.

3.1.4 Verification of side beam vorticity

Theory predicts that the side beams produced by these holographic masks should carry an OAM of order l in the first side beam, and increasing order of OAM for higher order side beams [58, 10]. These masks have produced side beams with doughnut intensity profiles typical of OAM beams, however this alone is insufficient to confirm the vortex property of the beam. The OAM and the vortex state are defined by the azimuthal phase dependence of the beam. The array from which the power spectra in figure 3.3 were obtained is complex–valued. This array can instead be plotted in terms of the argument of each point, to demonstrate the phase variation. The results of this can be seen in figure 3.5. We note that the central ring pattern in each subplot of figure 3.5, has no azimuthal phase variation, but only a π–phase shift between consecutive rings as the intensity has passed through a zero–intensity. The points found at $\pm 2.3 \mu rad$ are the doughnuts in figure 3.3, showing a variation of 2π around their axis. This demonstrates that the first intensity doughnuts are $l = 1$ vortex beams.

Additionally, it can be seen that in figures 3.5b and 3.5c, there is a 4π phase variation around a point found at $\pm 4.5 \mu rad$, corresponding to an $l = 2$ vortex found in the second

diffraction order. This feature is not found in figure 3.5a, agreeing with the results reported by Verbeeck *et al.* [6].

3.2 Aperture radius effects

It is well established in optics, that the propagation behaviour of experimental Bessel beams is unusual [49]. The experimental zero–order optical Bessel beam diffracts less than a Gaussian with the same initial central spot diameter [49]. The Gaussian beam used by Durnin [49] showed "measurable spreading after propagating only $1cm$", while the central spot of the Bessel beam used was unchanged in size over $1m$. This unusual property would be highly interesting to replicate in electron vortex beams. In our 2012 paper, it was found by us that aperturing the Bessel function and Laguerre–Gaussian functions at the first zero was insufficient to enable differentiation between the resultant beams as Bessel–like or Laguerre–Gaussian–like [63]. To work towards an electron Bessel beam, here we show the results of increasing the radius of the mask aperture to include more of the Bessel beam wavefunction.

This study was performed only for the Bessel wavefunction, as the Bessel beam has an infinite number of semi–regular zeros at which the masks could be apertured. The Laguerre–Gaussian beam has an arbitrary, finite number of zeros determined by $p+1$, and the position of the zeros is also affected by p. As p would need to be varied throughout this study, in addition to the aperture radius, it has been decided that this section will concentrate solely on the Bessel beam holographic mask.

3.2.1 Mask design

The radial aperture over the holographic mask was varied, by being set to coincide with the different Bessel zeros, from 1-5 and 10. This series enables us to see the progression of the sequence, followed by an extension of the concept up to the tenth Bessel zero. In figures 3.6–3.11 we can see the series of resultant masks, with their associated power spectra, and a phase map across the far–field.

At each of the zeros we note that the phase will change by π radians. This results in a change of sign in the interference pattern of the reference wave with the Bessel beam wavefunction. This is shown in the mask as a change from above average to below average regions, so when moving radially outwards, the mask changes from black to white (or vice versa) at the radius of the Bessel zero. This results in a chequerboard pattern in the mask.

The alternating pattern in the masks covering greater than one zero of the Bessel function are therefore more complex to manufacture as not all pieces are strongly connected. This difficulty could be overcome by using support bars in the mask construction, which would then need to be taken into consideration in interpreting the resulting intensity pattern of the mask.

The masks were all designed with the same binarisation level as discussed in section 3.1.1, and an aperture radius of $R_{max} = 42\mu m$. Other than the width of the Bessel wavefunction (which is controlled by the ratio of k_z to k_r), these masks are designed as described in section 3.1.1.

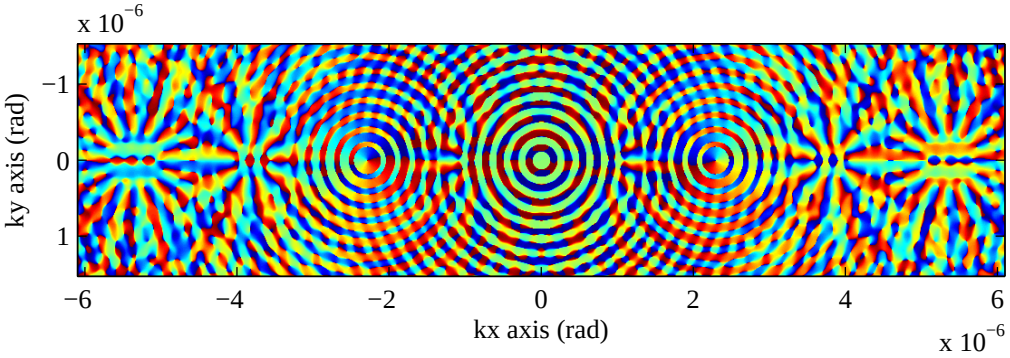

(a) Argument of top hat mask power spectrum

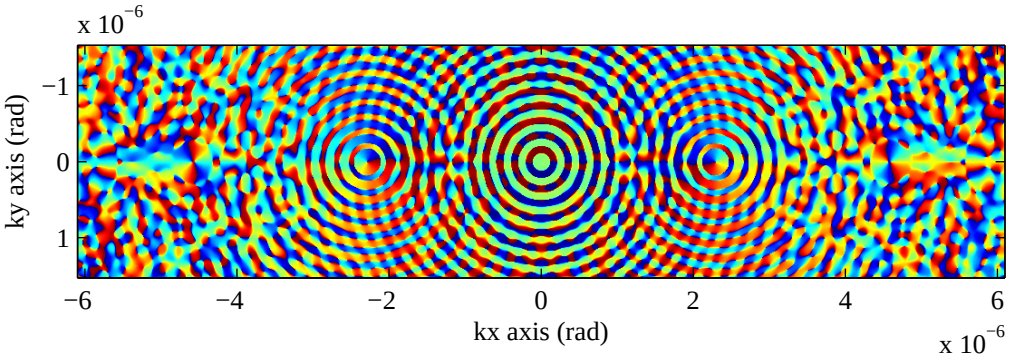

(b) Argument of Bessel mask power spectrum

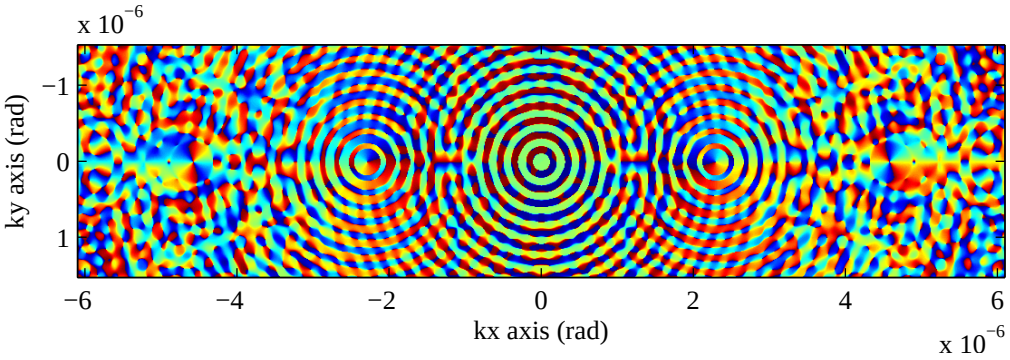

(c) Argument of Laguerre–Gaussian mask power spectrum

Figure 3.5: The phase across far field image of holographic masks using the different radial distribution functions. Red represents a phase of 0, while blue represents a phase of 2π.

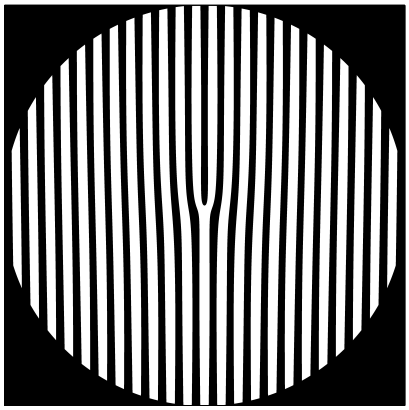

(a) Binarised mask

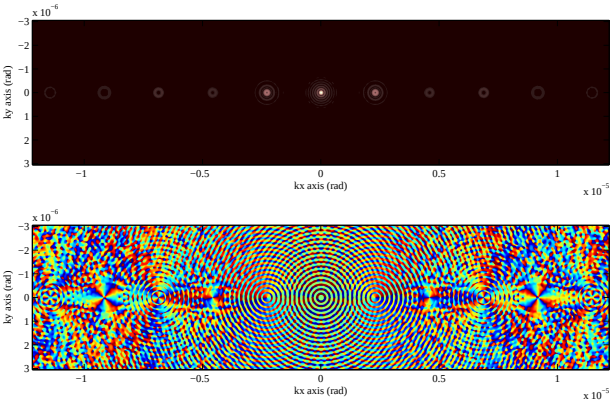

(c) Phase map of power spectrum

Figure 3.6: Mask and results of aperturing at the first Bessel zero

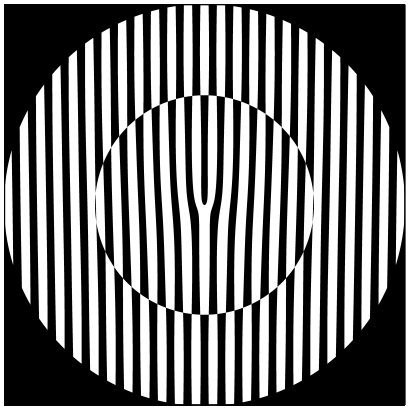

(a) Binarised mask

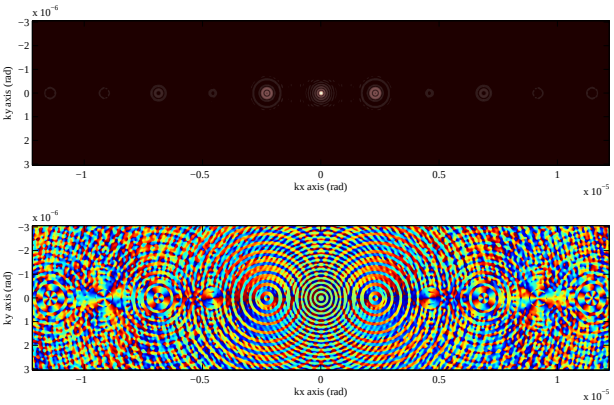

(c) Phase map of power spectrum

Figure 3.7: Mask and results of aperturing at the second Bessel zero

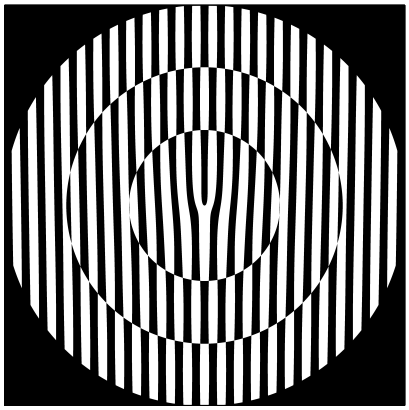

(a) Binarised mask

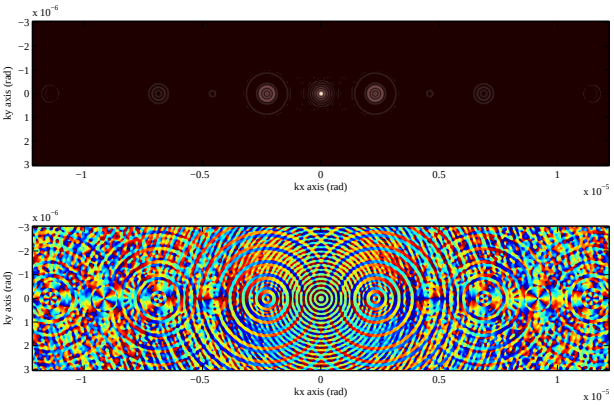

(c) Phase map of power spectrum

Figure 3.8: Mask and results of aperturing at the third Bessel zero

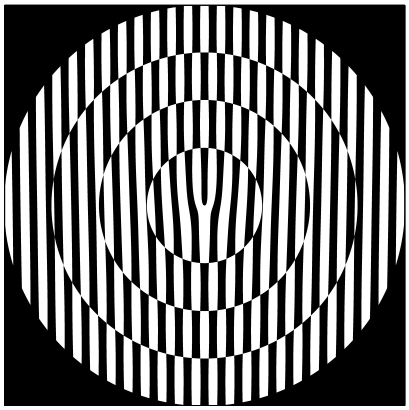

(a) Binarised mask

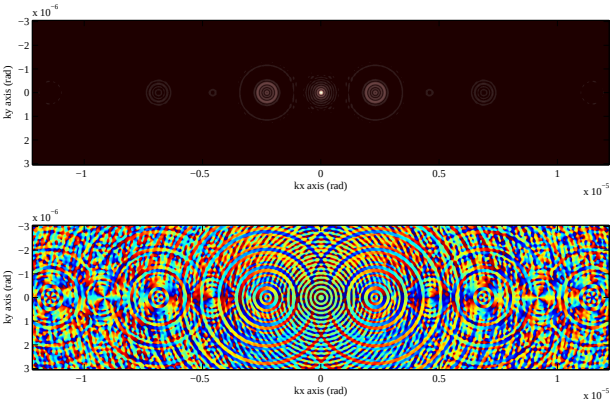

(c) Phase map of power spectrum

Figure 3.9: Mask and results of aperturing at the fourth Bessel zero

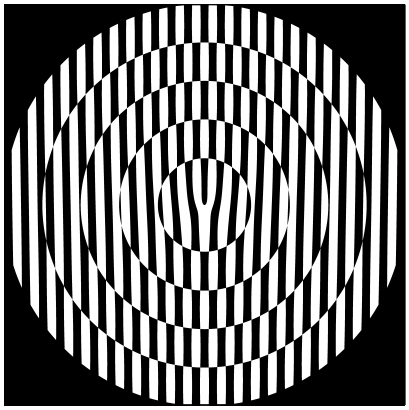

(a) Binarised mask

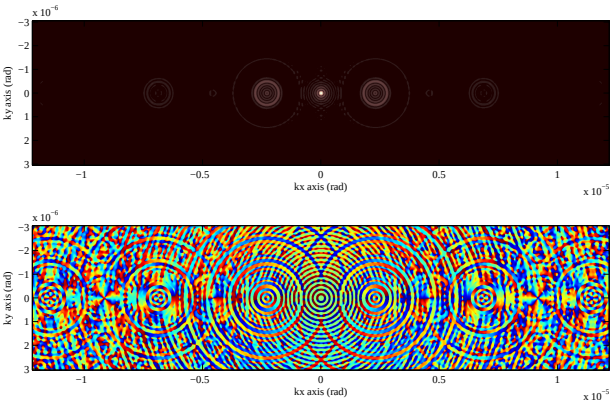

(c) Phase map of power spectrum

Figure 3.10: Mask and results of aperturing at the fifth Bessel zero

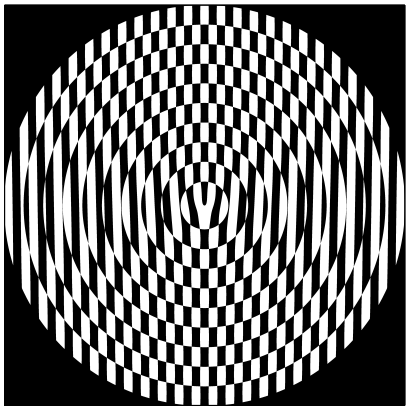

(a) Binarised mask

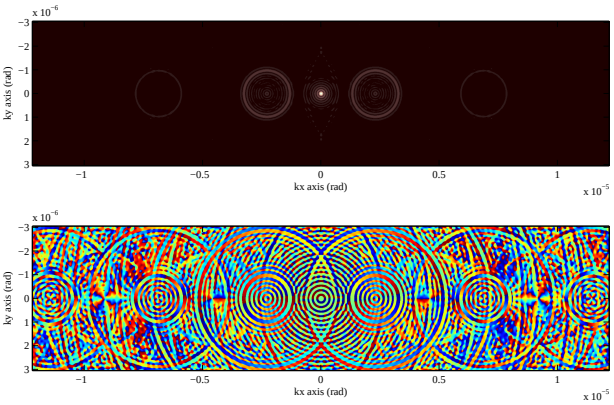

(c) Phase map of power spectrum

Figure 3.11: Mask and results of aperturing at the tenth Bessel zero

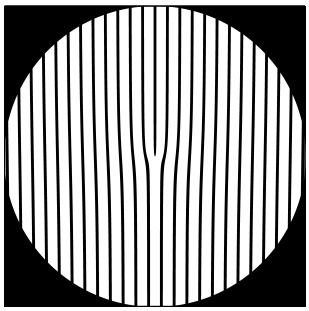

(a) Top hat mask, binarisation level 0.5

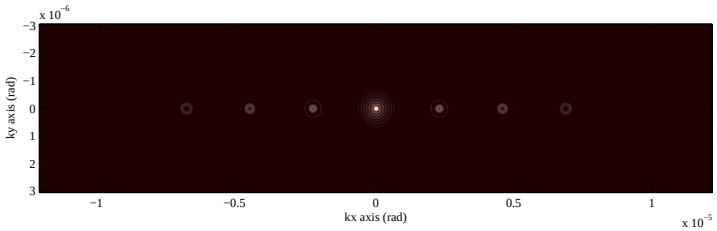

(b) Top hat mask power spectrum, binarisation level 0.5

Figure 3.12: Top hat mask and spectrum, binarised at 0.5

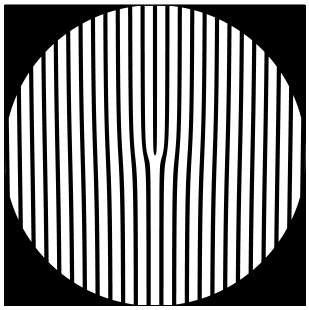

(a) Top hat mask, binarisation level 1.0

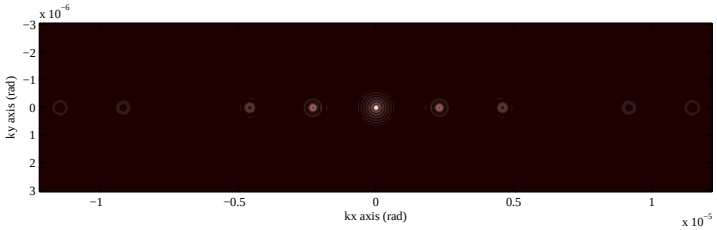

(b) Top hat mask power spectrum, binarisation level 1.0

Figure 3.13: Top hat mask and spectrum, binarised at 1.0

3.2.2 Theoretical far field results

As demonstrated previously, the far–field of the holographic masks can be simulated by performing a 2D Fourier transform on the mask. This has been carried out on the aperture–radius varied masks. The resultant power spectra and phase maps are produced in subfigures b and c of figures 3.6 to 3.11. The power spectra are produced in a pink colour map as this allows for clearer viewing of the side beams.

We can note that as the number of Bessel rings included is increased, the diameter of the 1^{st} order side beams increases. The radius of the apertures remained the same throughout and thus the larger sidebeams can be attributed to increased diffraction caused by the additional detail within the masks. The Fourier transform of the Bessel function is a delta function ring, and we see as more of the Bessel function is encoded into the mask prior to truncation, the far–field diffraction pattern tends towards the delta function ring.

The increased size of vortex beam from the same sized aperture however could be useful experimentally. The increased size would more easily enable a nanoparticle or similar to be illuminated by only part of a vortex without bringing in additional complications caused by defocussing, extending the currently available experimental techniques.

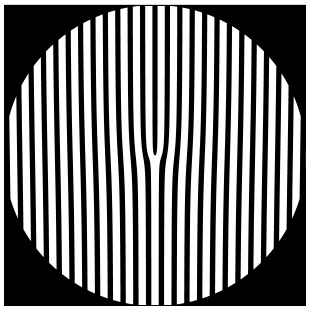

(a) Top hat mask, binarisation level 1.5

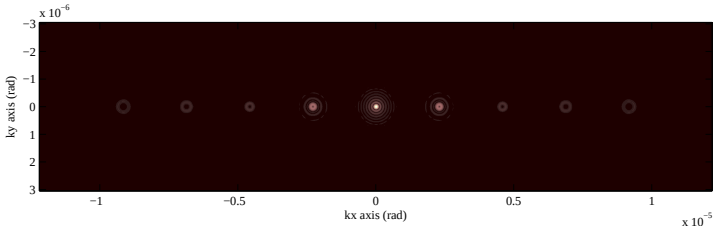

(b) Top hat mask power spectrum, binarisation level 1.5

Figure 3.14: Top hat mask and spectrum, binarised at 1.5

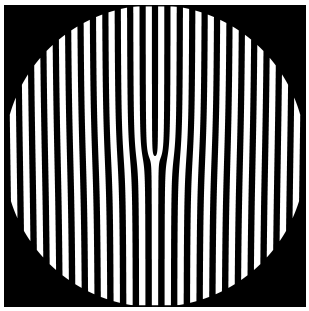

(a) Top hat mask, binarisation level 2.0

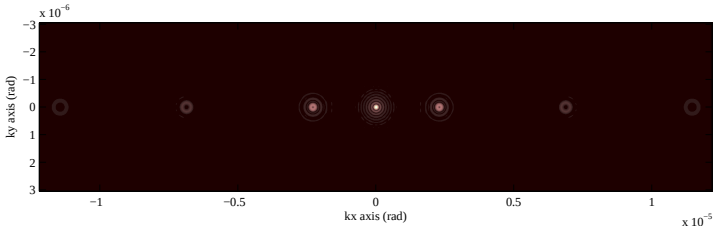

(b) Top hat mask power spectrum, binarisation level 2.0

Figure 3.15: Top hat mask and spectrum, binarised at 2.0

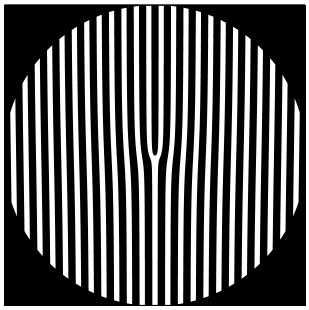

(a) Top hat mask, binarisation level 2.5

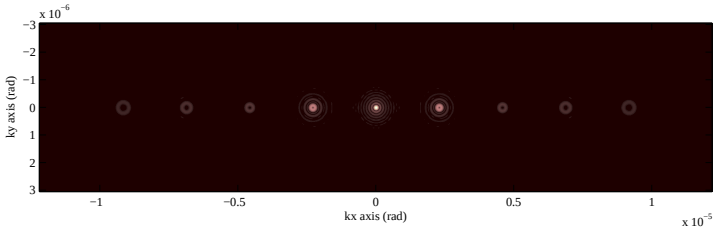

(b) Top hat mask power spectrum, binarisation level 2.5

Figure 3.16: Top hat mask and spectrum, binarised at 2.5

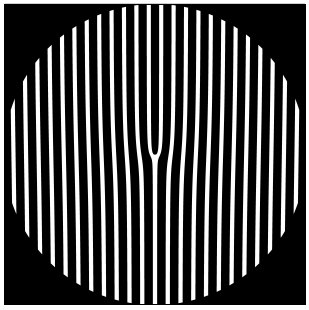

(a) Top hat mask, binarisation level 3.0

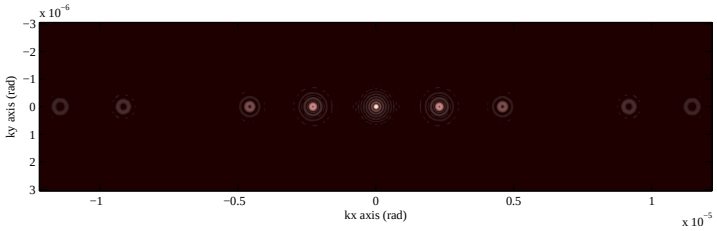

(b) Top hat mask power spectrum, binarisation level 3.0

Figure 3.17: Top hat mask and spectrum, binarised at 3.0

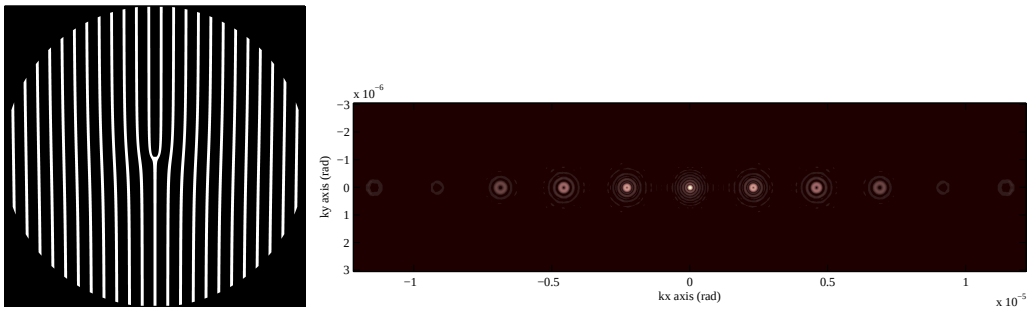

(a) Top hat mask, binarisation level 3.5

(b) Top hat mask power spectrum, binarisation level 3.5

Figure 3.18: Top hat mask and spectrum, binarised at 3.5

Figure 3.19: Colour bar showing the colour range of the power spectra. Normalised from 0 to 1

3.3 Binarisation level effects

As a further study developed from the challenges of efficient binarisation of the different radial distribution function masks, it was noted that changing the binarisation level affects the diffraction orders found in the far–field.

Here we note the effects of the binarisation level on the top hat mask and on the corresponding far–field diffraction pattern intensity. This binarisation variation study has only been performed for the top hat mask as its corresponding interference pattern is able to produce a connected mask with a strong fork feature across a broad variation in binarisation levels.

These masks have been produced as described in section 3.1.1, other than the choice of binarisation level. The binarisation function is designed such that regions with an intensity greater than the binarisation level are set to zero to allow beam passage. All other regions are set to a maximum opacity. The function from which the binarised mask is produced varies from 0 to 4, as the peak value is represented by $|1+1|^2$. A binarisation level of 0 results in an empty aperture which would trivially result in an Airy disc in the far–field with no OAM. A binarisation level of 4 results in a full aperture which would allow no intensity to pass.

Following the above, the binarisation level was varied across the range in steps of 0.5 excluding the two extremes which do not produce vortex beams. The masks resulting from this process, alongside their associated power spectra are produced in figures 3.12 to 3.18. The pink colour map of the power spectra is chosen to maximise side beam clarity, avoiding the need to display the data in an unphysical logarithmically–scaled format.

Comparing the masks, we note that as the binarisation level increases, the ratio of black to white (which would translate to foil and hole respectively in an experimental setup) increases. This decreases the area through which a beam can pass. To enable a comparison of mask structure shape, rather than comparing intensity–dependent results, the binarised masks are intensity normalised for this study.

Throughout this series, the basic form of the mask remains the same, with a two–

pronged form and an otherwise linear diffraction grating. Extending the diffraction grating analogue, we can consider the missing orders of side beam which can be noted amongst the power spectra of figures 3.12 to 3.18. These can be considered in terms of elementary geometric optics.

Treating the mask as a linear diffraction grating, and ignoring the fork defect in the present analysis, we can consider the coincidence of interference maxima (where the beams would lie), and diffraction minima (in this system corresponding to the zeros of the envelope Airy disc due to the round aperture). If we regard the slit width to be a, and the inter–slit spacing to be b, at certain ratios, the missing orders will appear with a noticeable regularity. When $a = b$, all the even diffraction orders will be missing. This system corresponds to subfigure 3.15a at a binarisation level of $1/2$ of the maximum. When $2a = b$ or $a = 2b$, every third order is missing. We see this at binarisation levels of 1.0 and 3.0, and can note the missing orders of figures 3.13b and 3.17b.

That the mask can be designed to select which orders will be created in the far–field holds great potential for experimental application. Following this study, it is possible to apply this technique in designing masks to select which vortex orders are adjacent. This would assist in having two or more vortices impinging on a nanoparticle or similar which could possibly be developed into systems similar to the optical vortex beam powered micro–motors [65].

3.4 Reference wave frequency effects

The frequency of the reference plane wave used affects the spacing of the lines seen in the holographic masks. This spacing is inversely related to the spacing of the side beams seen in the far–field. However, increasing the reference wave frequency also increases the level of detail with which the mask must be manufactured. Increasing this level of detail increases the time taken to produce the mask and means the resulting mask is more fragile and likely to need additional support bars.

At low frequencies of reference plane wave, the side beams in the experimental far–field may not be sufficiently separated and well defined, particularly due to microscope abberations. The masks however, cannot be produced with arbitrarily high–frequency reference waves. A balance needs to be found between high and low reference plane wave frequencies to enable a good quality experimental electron vortex beam to be produced. It is this requirement which motivates this last area of study of holographic mask design within this research.

3.4.1 Mask design to study reference wave frequency effects

To determine the ideal balance between far–field separation of beams, and ease of experimental production, we must first scale the angular spacing of the theoretical far–field to correlate with the real space experimental far–field in the electron microscope. This is performed as:

$$\tan\theta = \frac{y}{L} \tag{3.1}$$

$$\theta \simeq \frac{y}{L} \tag{3.2}$$

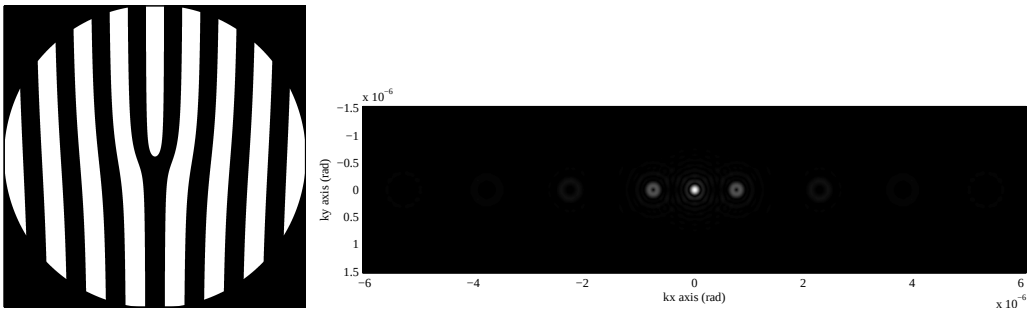

(a) Top hat mask,$\alpha = 8$ (b) Top hat mask power spectrum,$\alpha = 8$

Figure 3.20: Top hat mask and power spectrum, with grating number= 8

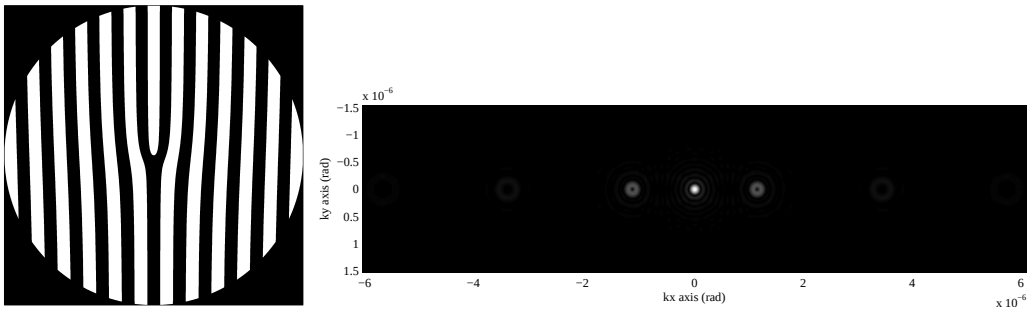

(a) Top hat mask,$\alpha = 12$ (b) Top hat mask power spectrum,$\alpha = 12$

Figure 3.21: Top hat mask and power spectrum, with grating number= 12

where θ describes the angular separation, in radians, y is the distance measured in plane between the centre of the pattern and the centre of the side beam, and L is the camera length (the distance between the aperture and the imaging screen), both measured in metres. L is determined through other experiments and has ben found by Dr Thirunavukkarasu Gnanavel in our experimental setup to be of the order of $10^{-2}m \pm 50\%$. In this equation, we have applied the small angle approximation, which is well justified as the angles involved in this system are of the order of milliradians.

The masks for this section are of the top hat type as they are the most regularly spaced and scale well under this modification. The slightly straighter tines in the top hat system also display most clearly when created at high plane wave frequencies. These masks are produced as described in section 3.1.1, in which the plane wave frequency is scaled as $k_p = {}^{\alpha\pi}/_{R_{max}}$. In the following results section we will refer to the prefactor α as the grating number.

3.4.2 Theoretical far field results

It is known from comparison with optical diffraction gratings that the separation in the far–field is directly proportional to the grating number used. This is clearly demonstrated to also be true with the modified diffraction grating presented as the holographic mask, seen in figures 3.20 – 3.23, in which the grating number is varied from 8 to 24.

Working with camera length $L = 10^{-2}m$, the position of the first side beams can be

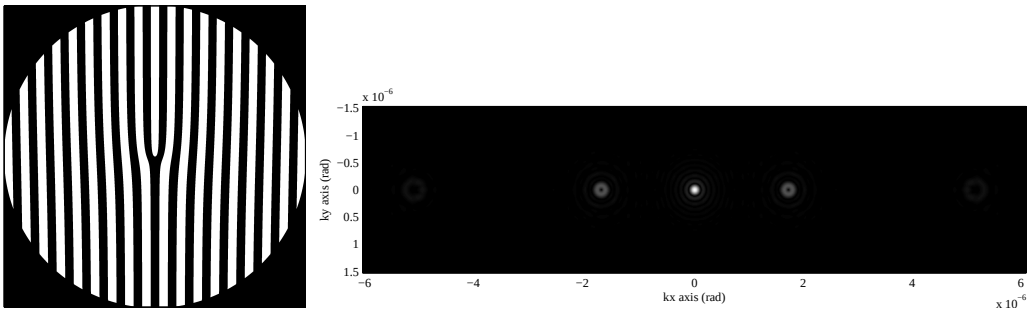

(a) Top hat mask,$\alpha = 18$ (b) Top hat mask power spectrum,$\alpha = 18$

Figure 3.22: Top hat mask and power spectrum, with grating number= 18

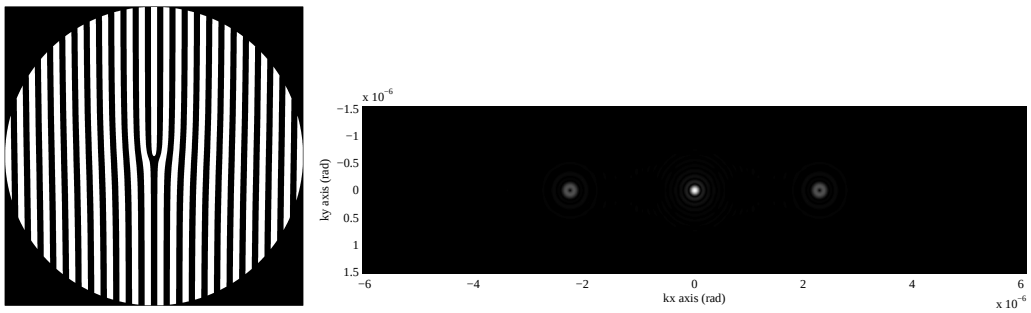

(a) Top hat mask,$\alpha = 24$ (b) Top hat mask power spectrum,$\alpha = 24$

Figure 3.23: Top hat mask and power spectrum, with grating number= 12

calculated to be expected at:

$$\alpha = 8, \qquad y = 7.9 \times 10^{-9} m \tag{3.3}$$

$$\alpha = 12, \qquad y = 1.1 \times 10^{-8} m \tag{3.4}$$

$$\alpha = 18, \qquad y = 1.7 \times 10^{-8} m \tag{3.5}$$

$$\alpha = 24, \qquad y = 2.3 \times 10^{-8} m \tag{3.6}$$

This range was calculated for mask radius of $R_{max} = 21\mu m$, to allow comparison with experimental results in York. An $\alpha = 8$, $R_{max} = 21\mu m$ mask has been produced and the mask and its resultant far–field intensity pattern can be seen in figure 3.24. The intensity pattern imaged here is slightly defocussed to allow for a clear view of the vortex features. The mask was fabricated, to the designs produced here, and the experiment performed by Dr Thirunavukkarasu Gnanavel. The experimental results are replicated here to demonstrate the accuracy of the theory.

From subfigure 3.24b we can note that the centre of the first vortex side beam is approximately $10nm \pm 10\%$ from the centre of the diffraction pattern. This is of the same order as the predicted $7.9nm$ but is still substantially different. To improve the relationship between prediction and experiment, it is first key to determine the camera length with more accuracy, although this is a difficult process to perform.

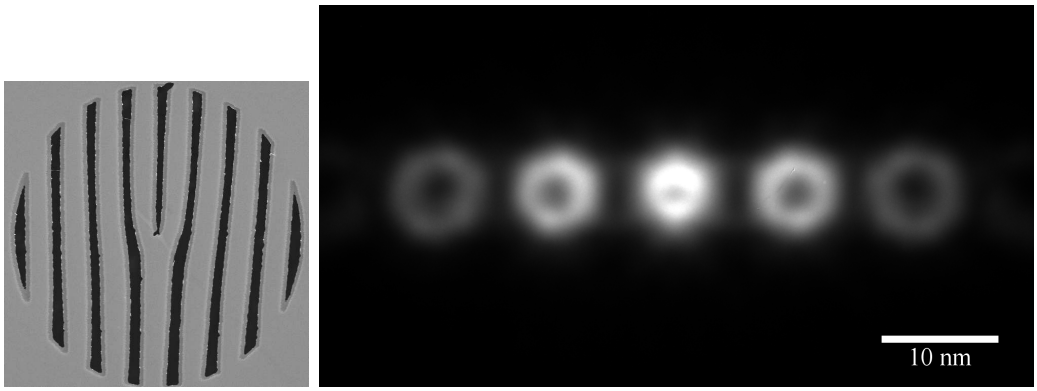

(a) Top hat mask,$\alpha = 8$ (b) Top hat mask intensity pattern,$\alpha = 8$

Figure 3.24: Experimental mask and power spectrum, with grating number= 8

3.5 Holographic mask study summary

In this chapter, the parameter space of holographic mask production was explored. Each section investigated the variation of a different parameter and produced results to assist in future design of experimental holographic masks for production of electron vortex beams.

When considering the application of the radial distribution function, it was found that of the options, to maximise intensity in the first–order side beam, a top hat function mask is preferable to Laguerre–Gaussian or Bessel funtion modulated masks, giving up to 12% higher peak intensity. Alternatively, if all orders of sidebeams are desired present in the far–field, a top hat mask is not suitable, while Laguerre–Gaussian and Bessel masks are. It was also found that within current experimental limits, the Laguerre–Gaussian and Bessel function modulated masks are indistinguishable.

Within the Bessel function modulated holographic masks, the range of the function included within the mask aperture was varied. It was found that increasing the range of the Bessel function included in the mask production, increases the radius of the sidebeams in the far–field of the mask and the doughnut intensity profile narrows towards a delta–function ring, which is expected as the Fourier transform of an ideal Bessel function. This ability to vary the radius of sidebeam in the far–field could potentially be employed as a coarse control of beam size, although presently would be limited by the experimental difficulty of producing such masks.

In section 3.3, the binarisation level used to produce the top hat mask was varied. This theory confirms as could be expected from geometric optics that binarisation at exact fractions of the maximum value result in the set of far–field beams missing orders in regular patterns. Although simple, this knowledge can be employed experimentally to enable select orders of beam to be adjacent for potential nanomanipulation applications.

The final section of this chapter considered a variation of the plane wave frequency used in the production of the mask. This is important for optimising the spacing of the vortex beams in the far–field, with sufficiently robust masks. The limits of the fragility of the mask will dependent on the resolution of the cutting machine used, and the material properties of the sample foil, when these limits are known, the far–field placement can

be predicted to determine whether the spacing between beams is sufficient.

Chapter 4

Simulating electron vortex beam propagation

The behaviour of the electron vortex beam is at its most interesting when the whole 3D structure can be seen and analysed and understood. The mask and far–field images alone do not highlight some of the key aspects of the holographic mask – vortex beam system. The research in this chapter was conducted in order to connect the illuminated mask to the resultant electron vortex beams. This study also enables an understanding of the structural properties of the vortex beams, such as Rayleigh length and waist size. Knowledge of these properties is indispensable in applying the electron vortex beam as an experimental tool for manipulation and trapping of nanoparticles.

We begin by reviewing the application of Fresnel propagation theory to electron microscopy, with regards to section 2.5. This is followed by a discussion of electron beam propagation within the TEM in both near–field (immediately behind the mask) and far–field (near the focussed diffraction pattern).

4.1 Theory of electron vortex beam propagation

A number of methods exist to model electron beam propagation within electron microscopy. These inclused Bloch wave methods, Monte Carlo methods and multislice methods [59, 66]. In this research a free-space version of the multislice method was applied.

The multislice method was chosen as it is most adaptable to the complex structure of the forked mask, and the resultant set of electron vortices. The propagation is chosen to be modelled in free space rather than through a sample (as in [41]) as we wish to study the formation of the vortex following the mask, within the vacuum of the microscope chamber, and the behaviour of the vortex beams in free space.

The multislice method typically models the propagation of a beam through a crystal sample, in which the sample is considered as a set of 2D slices wherein the sample potential due to each atom can be considered to lie in one of a set of planes. Between these samples, the beam is propagated through a short region of vacuum before interacting with the next sample slice. This is performed by cyclically applying a transmission function

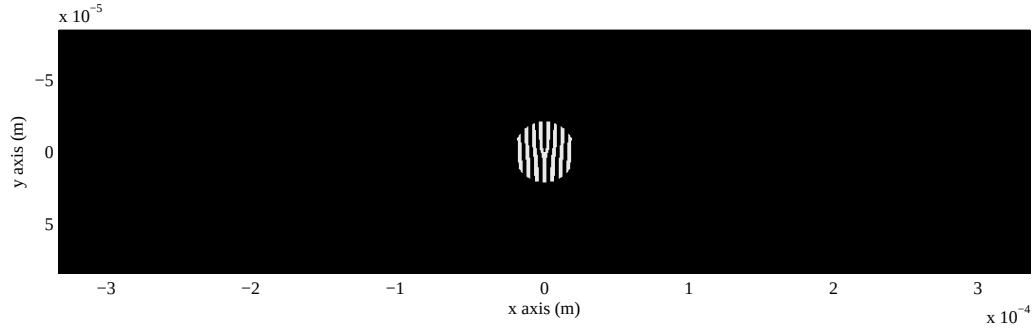

(a) Intensity pattern

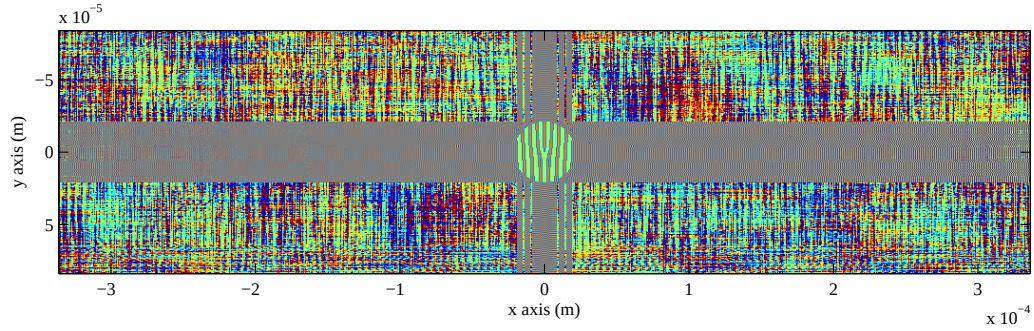

(b) Phase map

Figure 4.1: The intensity pattern and phase map of the mask at $df = 1 \times 10^{-9}m$

to the wavefront, representing the effects of the sample on the beam, followed by a vacuum propagation operator. In free space propagation, the transmission function can be considered as a multiplication by one.

In the free space limit, the multislice method reduces to the Fresnel propagation methods of classical optics as discussed in section 2.5, and was first derived by Cowley and Moodie in 1957 [67]. The Fresnel propagation method applies an operator to the wavefunction with a factor Δz, which calculates the wavefunction a small distance further along the optic axis of the system. Repeated application of the propagation operator allows for modelling along the length of the beam, with limits due to the levels of approximation in the propagation operator, primarily that the spherical wavefronts (from Huygens' principle) are modelled as parabolic. This leads to an error of order $\mathcal{O}(\Delta z^2)$ [59].

We first consider the beam in the near–field of the mask, and the effect of defocus on the intensity and phase in section 4.2. This is followed by the results and discussion of propagating the beams in the far–field in section 4.3.

4.2 Mask defocus

In this section the results of a propagation simulation applied to a holographic mask are presented. The mask is a $42\mu m$ diameter, $l = 1$ top–hat mask with a grating number of 8, as defined in chapter 3.

In an experimental TEM set–up, the holographic mask in the condensor plane is illuminated by a planar electron wavefront.

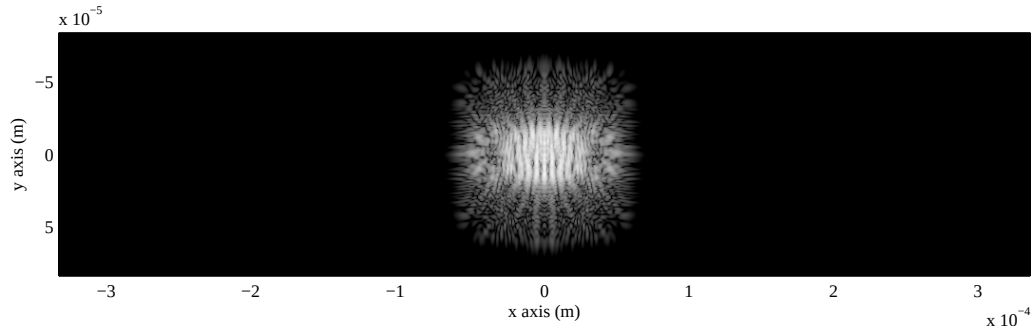

(a) Intensity pattern

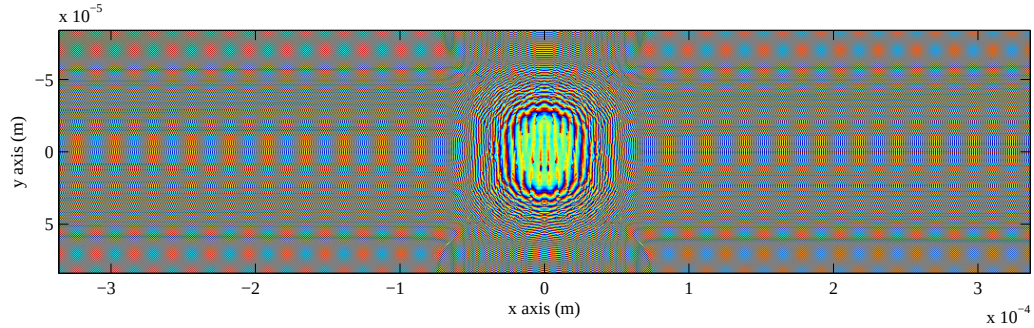

(b) Phase map

Figure 4.2: The intensity pattern and phase map of the mask at $df = 7.5m$

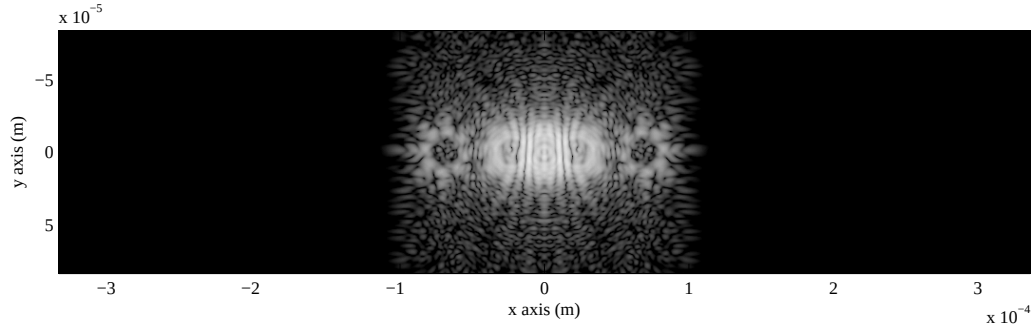

(a) Intensity pattern

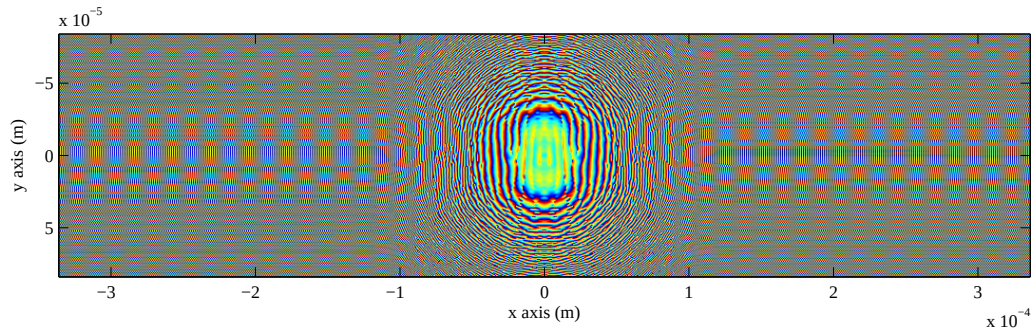

(b) Phase map

Figure 4.3: The intensity pattern and phase map of the mask at $df = 15m$

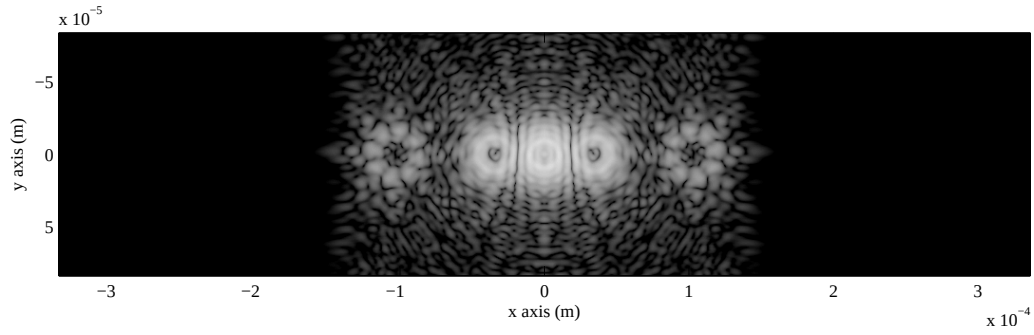

(a) Intensity pattern

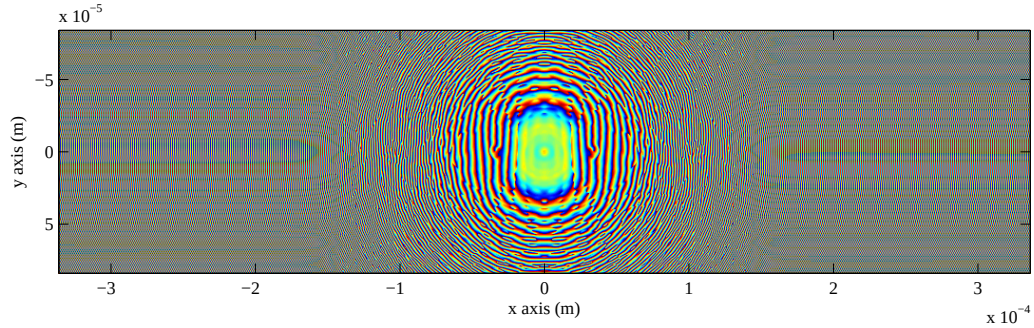

(b) Phase map

Figure 4.4: The intensity pattern and phase map of the mask at $df = 23m$

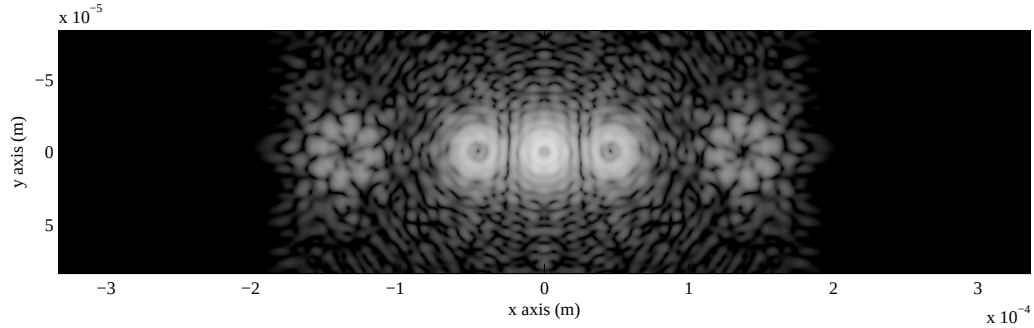

(a) Intensity pattern

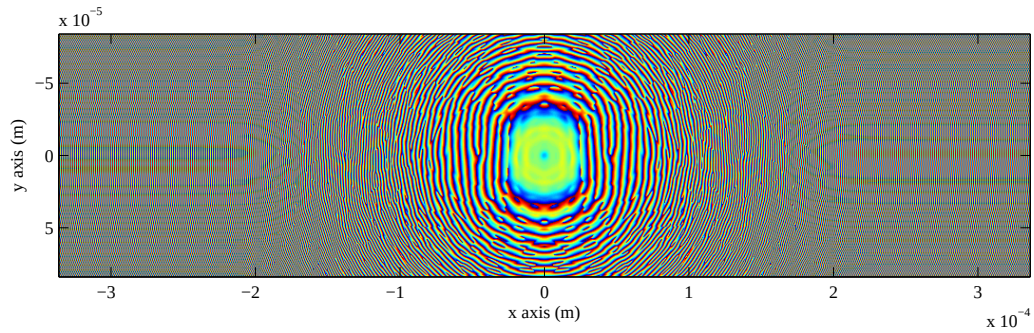

(b) Phase map

Figure 4.5: The intensity pattern and phase map of the mask at $df = 30m$

The series of images in figures 4.1–4.5 show the simulation of the propagation of an electron wave from $1 \times 10^{-9}m$ in figure 4.1 to $30m$ behind the mask, in figure 4.5. This is not a realistic situation, as within the microscope, lenses are used to image the far–field, rather than affording such long propagation distances, however, the simulation does give an impression of the formation of the far–field structure. The intensity maps are displayed on a logarithmic scale in order to show the maximum structural detail of the propagation series. These are produced in a grayscale, where white represents the maximum intensity, and black is the minimum intensity. The accompanying phase maps are shown in a rainbow colour map where blue represents a phase of $-\pi$ and red represents a phase of π.

Immediately behind the aperture (when the defocus value ≈ 0), the intensity pattern reproduces an image of the aperture itself, as seen in figure 4.1(a). The associated phase map (figure 4.1(b)) is also very simply explained; in the central area where there is intensity, the phases are approximately one of $0, -\pi, \pi$, the zero phase points are of very low intensity, and the regions of $\pm\pi$ are results of the first steps of a Fresnel propagation performed upon an array, which previously had a flat phase encoded. The Fresnel propagator is valid in the near–field of the propagation, $N_F = \frac{a^2}{L\lambda} \leq 1$ [60]. Where N_F is called the Fresnel number, a^2 is the characteristic aperture size, L is the defocus length, and λ is the wavelength.

As the propagation distance increases (also referred to as the defocus length), the intensity pattern defocusses accordingly, creating the series seen in figures 4.2–4.5. If the system was allowed to propagate freely over a long distance, the intensity pattern would approach that of the predicted far–field image. This can be seen in the intensity pattern of figure 4.5, when comparing with the far–field images of chapter 3.

The propagation of the phase maps enables the consideration of the vortex formation process. A vortex point can be considered to exist when all phases from $-\pi$ to π converge at one point in a smooth gradient. In figures 4.1(b) and 4.2(b), there are no clearly defined points of vorticity. In the counterpart intensity patterns in figure 4.1(a) and 4.2(a), it can be noted that no ring shaped intensity is apparent at the smaller values of defocus. The sidebeam vortices begin to become distinct over a defocus of $15 - 30m$, as seen in figures 4.3–4.5.

In addition to the sidebeam phase discontinuities, which are persistent over the defocus length used here, there are many additional points of phase discontinuity which can be seen in the phase maps. These are typically in broader areas of very low intensity, in patterns resembling speckle interference [30]. These do not persist throughout the propagation and annihilate with discontinuities of the opposite handedness over a very short propagation series [68]. It does not seem possible from the phase maps alone to determine which vortices are short lived and which vortices will be sustained until the far–field.

By a defocus of $30m$ (figure 4.5) the intensity pattern is clearly approaching the far–field intensity pattern. The first order sidebeams are visible and have a strong phase variation pattern around them.

In the true experimental setup, however, the electron beam does not propagate far behind the mask before reaching the objective lens, focussing the beam to converge to the far–field pattern, in the image plane.

4.3 Far–field defocus

The image focussed in the back focal plane of the objective lens is an approximation of the true far–field of the holographic mask. This is represented in this model, as discussed in chapter 3 by a 2D discrete Fourier transform of the mask. Propagating this plane along the optic axis of the TEM enables an understanding of the structure of the vortex beams in the typical planes in which they are applied in experiments.

A series of simulated intensity plots are produced in figure 4.6 showing the intensity of the beams in the image plane when defocussing over a range from $4.2 \times 10^{-22}\, m$ to $3.0 \times 10^{-6}\, m$.

We note firstly that for the smaller values of defocus (figures 4.6b and 4.6a), the intensity pattern shown is strongly similar to the pure far–field images produced in the earlier studies. The side beams have clear central minima and a distinct doughnut intensity profile.

At the higher values of defocus, the Fresnel fringes appearing begin to obscure the vortex features, which can be noted by the destruction of the doughnut intensity profiles at the higher values of defocus. These intensity maps are produced with an angular spacing, but can be scaled to predict the spacing and behaviour of the side beams if the size of the experimental defocus step can be determined from other experiments.

At the highest values of defocus, fork features can be seen to either side of the central beam, as in figures 4.6g and 4.6h. These forks are due to the interference of the $l = \pm 1$ side beams with the central, $l = 0$ order beam, and thus can be seen as variant of interferometry. The interference patterns at high defocus can be used as a method to verify the vorticity of first order side beams, and is easily experimentally achievable [61].

The following section describes the comparison of the theoretical work produced within this study with the experimental results provided by Dr Thirunavukkarasu Gnanavel[46].

4.4 Experimental comparison

In figure 4.7, we show a series of experimental images captured within an aberration–corrected TEM. These have been produced with increasing amounts of defocus, measured in ‘steps’ in the electron microscope. There is currently no method to exactly quantify the size of the defocus steps to allow for a quantitative comparison with the theoretical results, so the following discussion is necessarily restricted to a qualitative comparison with the theoretical results of figure 4.6.

The most notable difference between the theoretical and experimental series is the much less intense second–order sidebeams in the theoretical series, when compared with the experimental series. This has been traced to be a result of the imperfect mask cutting. Figure 4.8 displays the theoretical mask, an image of the experimental mask, and a computationally binarised image of the experimental mask. The most significant differences between the different masks are at the edges of the cut regions, as there are regions of experimental mask that have been thinned by the cutting process, but not entirely removed. We cannot know from the image in figure 4.8b, how thick these areas are, and thus how these might pass or block electrons. To approximate this mask, a 50% cutoff binarisation process was performed and is shown in figure 4.8c.

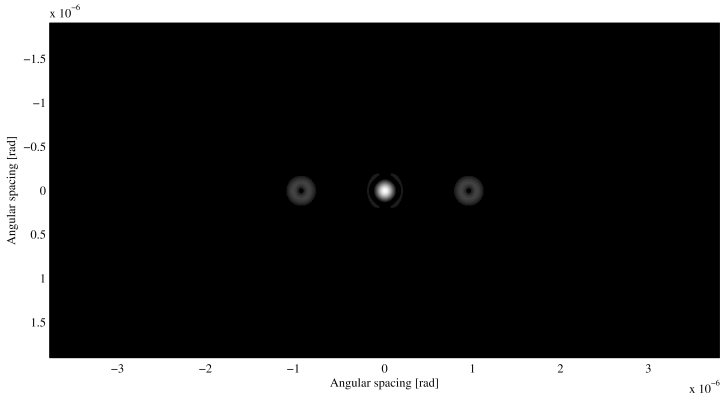

(a) Theoretical $df = 4.2 \times 10^{-22} m$

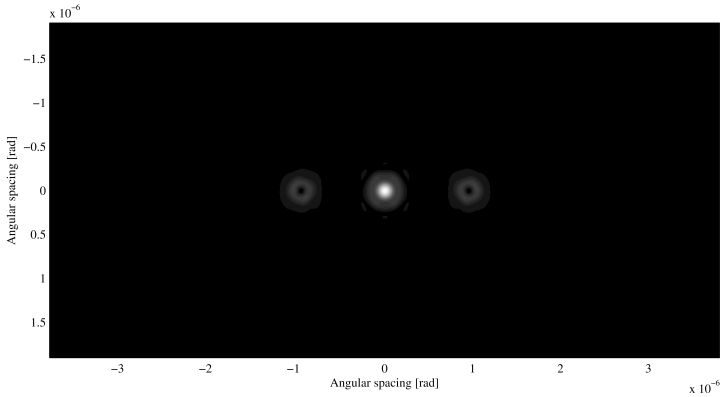

(b) Theoretical $df = 4.3 \times 10^{-7} m$

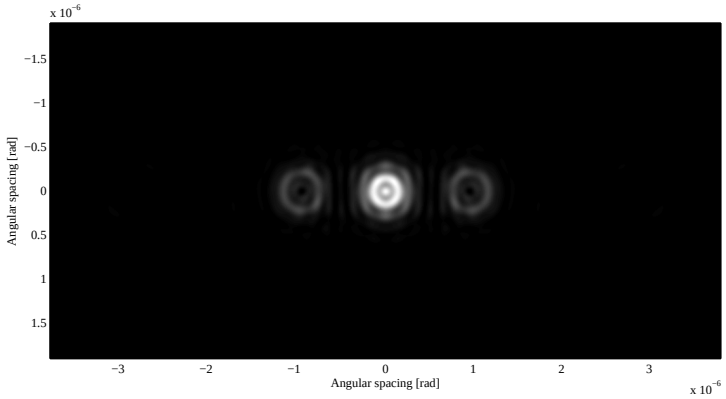

(c) Theoretical $df = 8.6 \times 10^{-7} m$

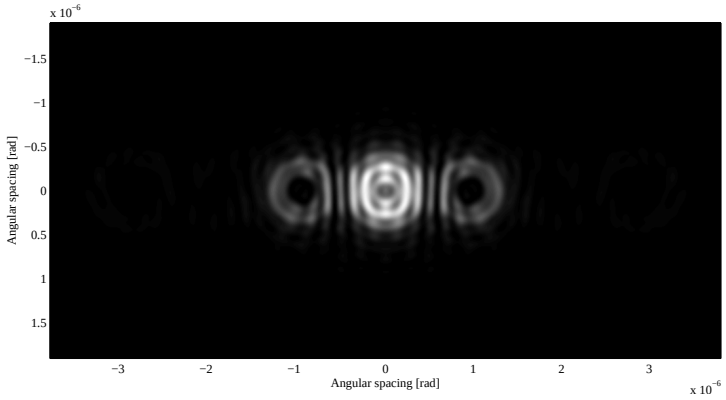

(d) Theoretical $df = 1.3 \times 10^{-6} m$

Figure 4.6: Simulated images of defocussed far–field of $l = 1$ Bessel mask

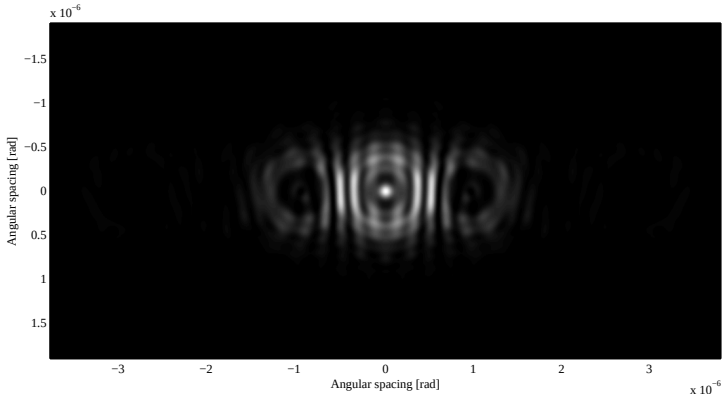

(e) Theoretical $df = 1.7 \times 10^{-6} m$

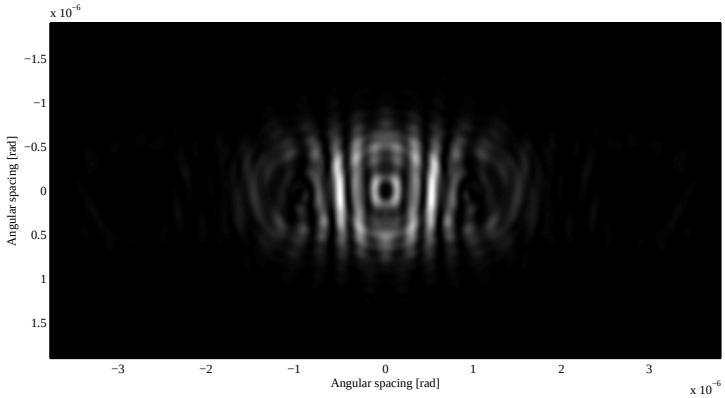

(f) Theoretical $df = 2.1 \times 10^{-6} m$

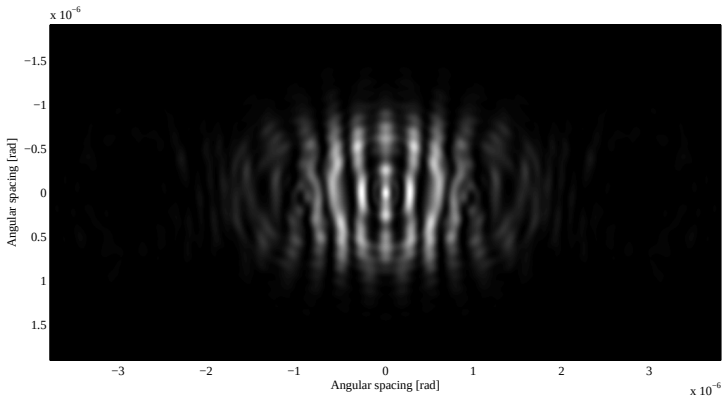

(g) Theoretical $df = 2.6 \times 10^{-6} m$

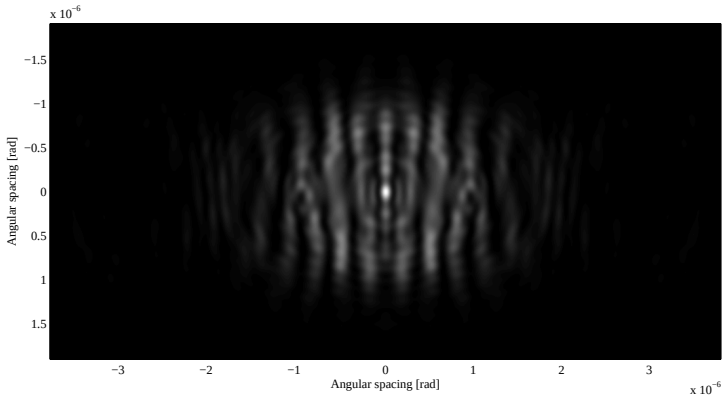

(h) Theoretical $df = 3.0 \times 10^{-6} m$

Figure 4.6: Simulated images of defocussed far–field of $l = 1$ Bessel mask

(a) Experimental focussed image

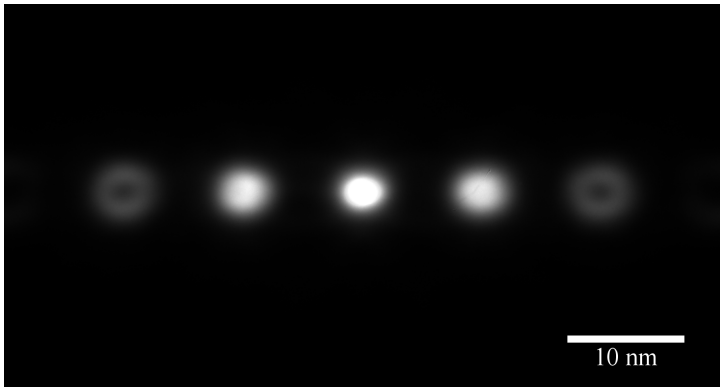

(b) Experimental $df = 1$ defocus steps

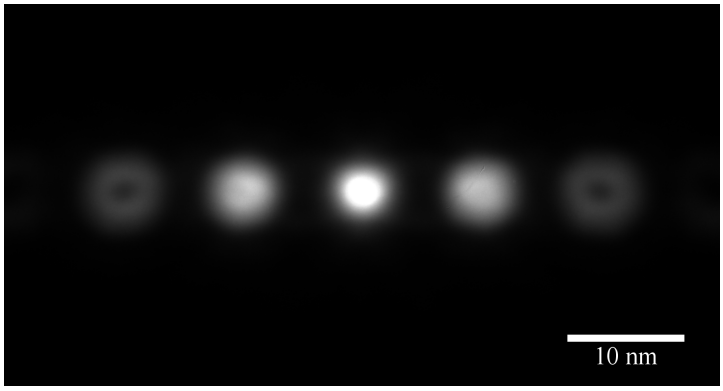

(c) Experimental $df = 2$ defocus steps

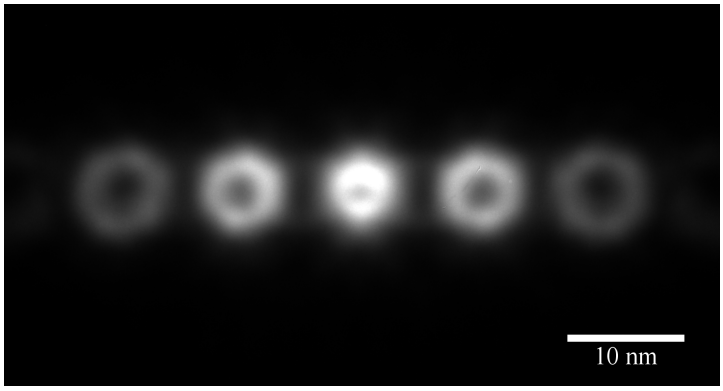

(d) Experimental $df = 3$ defocus steps

Figure 4.7: Experimental results of defocussed far–field of $l = 1$ Bessel mask

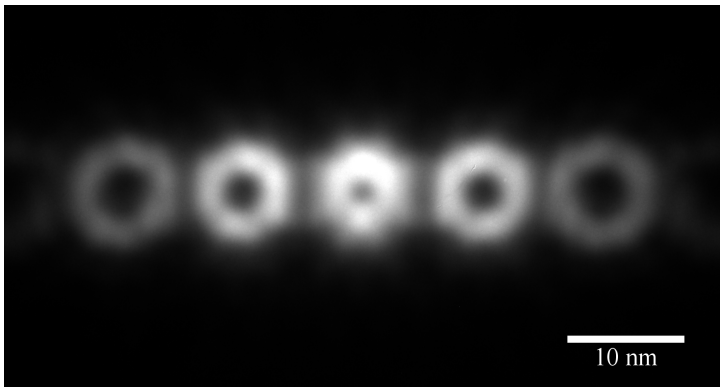

(e) Experimental $df = 4$ defocus steps

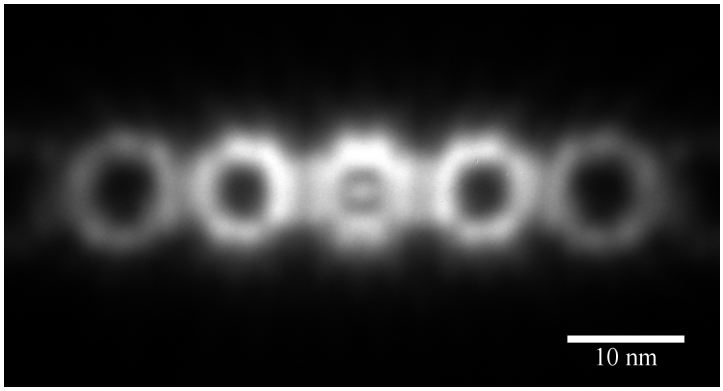

(f) Experimental $df = 5$ defocus steps

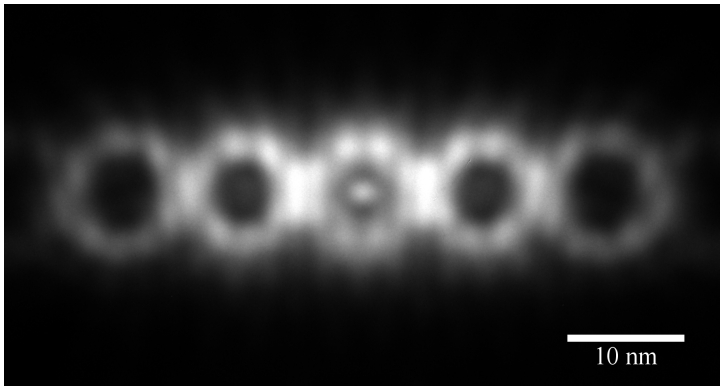

(g) Experimental $df = 6$ defocus steps

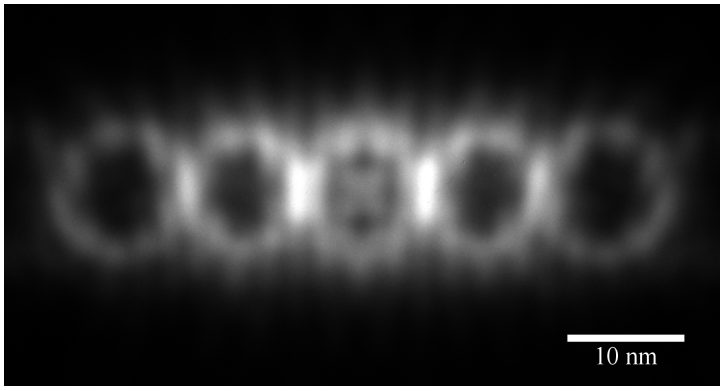

(h) Experimental $df = 7$ defocus steps

Figure 4.7: Experimental results of defocussed far–field of $l = 1$ Bessel mask

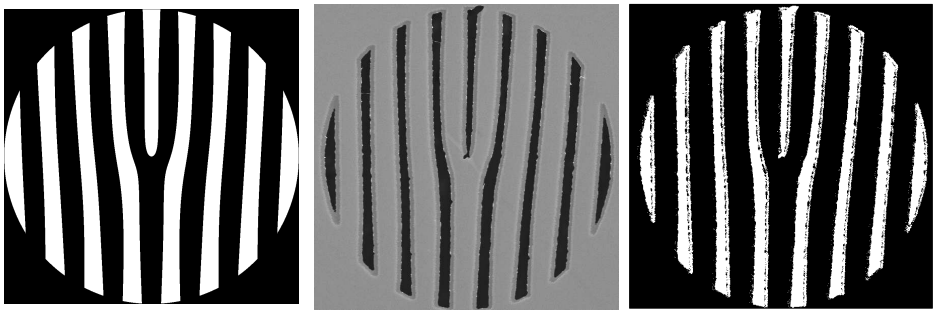

(a) Theoretical Bessel mask (b) Experimental Bessel mask (c) Computationally binarised, experimental mask

Figure 4.8: Images to compare theoretical and experimental mask production

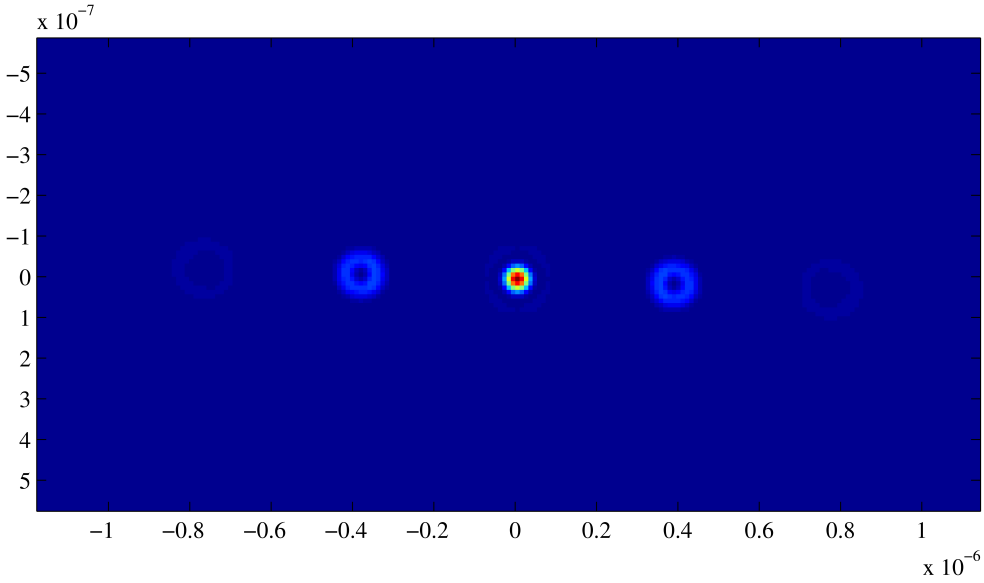

Figure 4.9: The simulated far–field image of the experimental mask

A simulation of the far–field of the experimental mask can be seen in figure 4.9. This clearly contrasts with the theoretical results of figure 4.6 as second–order sidebeams are visible, as in the experimental defocus series shown in figure 4.7.

Further comparing the theoretical and experimental defocus series, we note that in figures 4.7a–4.7b, there are no central minima visble in the first order sidebeams of the experimental data, while in equivalent low values of defocus in the simulated data, central minima are visible. This is an expected result, as due to the imperfectly coherent electron source, we expect experimental data to be broader than comparable theoretical data. This broadening covers over the narrow central minima, which becomes visible in the experimental data at higher values of defocus, when the central minima features are also broader. This is discussed by Schattschneider *et al.* in their analytical electron vortex beam paper [34].

4.5 Summary of propagation studies

In this chapter, propagation of both the near–field and the far–field of the holographic mask was studied. The simulated results of far–field propagation was compared with an experimental defocus series.

In the near–field propagation series the intensity doughnut profiles could be observed, albeit interference with overlapping diffraction orders has lead to modulation of the intensity around the doughnut. A corresponding $2\pi l$ phase discontinuity found within them. It was found that in the near–field regime, the rate of change of phase around a discontinuity was not at a constant rate.

In the far–field propagation series, the size of the intensity profile varies as expected from classical diffraction studies. This can be applied in experimental settings to give a fine control of the ring size in manipulation experiments. Combining this fine control with the coarse control gained with the results of varied Bessel function–range masks in section 3.2 would enable fine control over a large range of electron vortex ring sizes.

This propagation series was qualitatively compared with experimental results. Higher order sidebeams were visible in the experimental results, which was found to be due to inaccuracies in the mask cutting, while the absence of intensity minima in the centres of sidebeams at low values of defocus can be ascribed to beam incoherence, following Schattschneider *et al.* [34].

Chapter 5

Effect of aperture shape

5.1 Introduction and Literature Review

This section of the work was inspired as an extension to the previous sections through collaboration with Dr Jo Verbeeck of the University of Antwerp. The present work considered the effect of non–standard aperture designs on the far–field vortex behaviours, such as off–centred designs, or non–round apertures.

Round centred, and off–centred apertures were considered alongside triangular and square apertures. These were first applied over a single phase discontinuity to simulate applying the aperture over an existing vortex beam at a stage in the electron microscope after the holographic mask.

This was followed by applying the aperture functions in the creation of the holographic masks in order to simulate a more achieveable experiment and to combine the holographic results with the effect of the alternative apertures.

Similar apertures have been applied recently in the optical vortex beam regime [69, 70], and have been found to produce interesting results with a strong potential for application. The interest in unusual aperture shapes applied to optical vortex beams strems from a desire for a simple method to measure the OAM of a beam. In 2009, annular apertures were first applied to measure the OAM of a beam [71]. In the far–field of an annular aperture, an approximation to a Bessel beam will form. As shown in figure 2.1, the intensity pattern of a Bessel beam is dependent on the order of OAM and thus the position of the maxima can be used as a tool to measure the order of OAM of the beam.

It was later found by Hickmann *et al.* and developed further by Mourka *et al.* that applying a triangular aperture across a vortex beam results in an intensity pattern of dots, in which the number of dots is directly related to the order of OAM of the input beam [69, 70]. They were also able to use the aperture to determine the handedness of the beam, as this was also found to affect the intensity pattern seen in the far–field of the triangular aperture [69].

The triangular pattern of intensity dots also forces a division of high–order vortex beams into an array of $|l| = 1$ vortices, which lie between the intensity maxima of the triangular dot pattern. To extend this concept further, we also applied a square aperture towards the same aim, finding a repeated splitting of high–order vortices into lower order

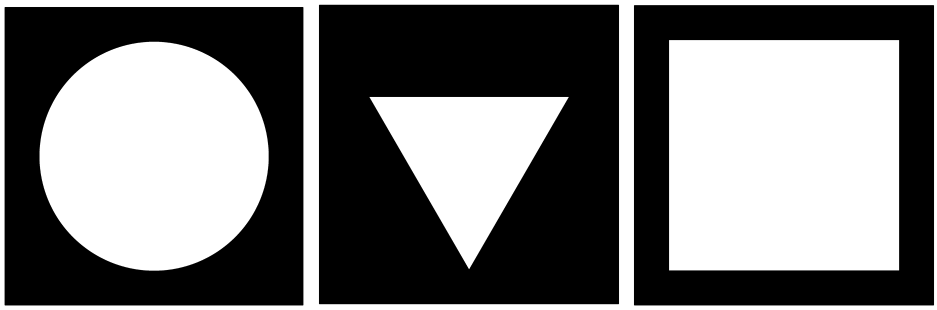

(a) Round aperture (b) Triangular aperture (c) Square aperture

Figure 5.1: The aperture shapes applied to the ideal vortex beams state

beams. These splitting patterns in both triangular and square cases appear in such a way as to obey both the symmetry imposed by the aperture and the structure imposed by the vortex.

The enforced splitting of high–order vortices provides a simple way to measure the order of OAM of a vortex beam, in a method which could easily be applied within an electron microscope. Arrays of optical vortices are used in biological sciences and colloid studies to control and manipulate large numbers of particles simultaneously [65, 72]. Arrays of electron vortices could become a crucial tool in manipulation of multiple nanoparticles within the field of electron microscopy.

In addition to the geometric apertures applied, the off–centred round aperture was also considered to investigate the persistence of vorticity under perturbation. This is a useful parameter to understand when considering the experimental implications of imperfect masks.

We begin by considering the effects of each of the apertures on a vortex beam by simulating the resultant far–field power spectra and phase masps. This is followed by a section considering the effects of such non–standard apertures applied as part of the vortex mask structure.

All results presented in this chapter are for systems where $l = 3$. This was chosen as this value allows all the features discussed to be observed while avoiding the unneccessary complexity of yet–higher orders.

The chapter concludes with a discussion of the results found through these studies and a look towards their future employment in experimental situations.

5.2 Aperturing a pure beam

5.2.1 Apertures

We begin this study by considering the aperture shapes applied. The circle, equilateral triangle and square are among the simplest of geometric shapes. These were chosen to be studied as by virtue of being simple geometric shapes, they also have easily predictable and well understood far–field intensity patterns. The apertures are shown in figure 5.1 and all are built around either radius or side length of $R_{max} = 21\mu m$ as in previous chapters.

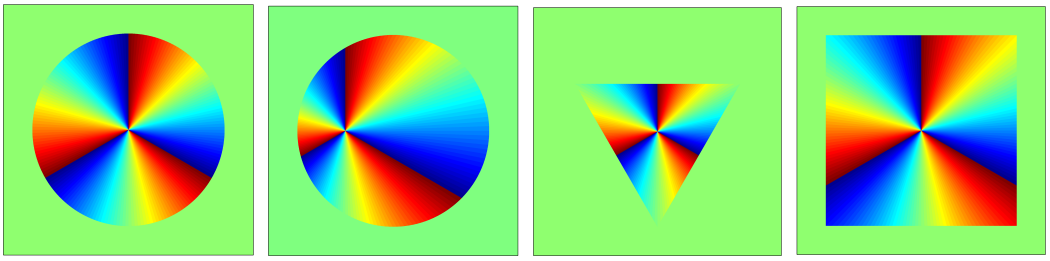

(a) Centred, round aperture (b) Off–centred, round aperture (c) Centred, triangular aperture (d) Centred, square aperture

Figure 5.2: The phases of the beams applied across the aperture shapes

The vortex phase structure was applied centrally across all of the apertures and additionally applied off centre of the circular aperture, with the phase vortex centred half–way between the aperture and its leftmost edge. These examples are shown in figure 5.2. The input vortex structures are all for the $l = 3$ case, as discussed in section 5.1.

These simulations are the equivalent of applying an aperture in the electron microscope column after the holographic mask aperture, over a single sidebeam. This would be challenging to perform experimentally as this would require accurate alignment of the two apertures and initial electron beam. This method of vorticity determination however, is simpler and more flexible than current methods used to determine the order of OAM of the beam, which requires the counting of fork prongs in interference patterns. The benefit of these simulations is that they allow for a clear understanding of the effect of the aperture shape upon the electron vortex behaviour.

5.2.2 Far–field results

The effects of these novel apertures can be shown in their far–field intensity and phase distributions. We discuss here the far–field intensity and phase profiles of each of the apertures, described above, in turn.

The first case of the centred, round aperture produces a doughnut intensity profile in the far–field, as would be expected. The phase variation across this array shows a constant rate of change of phase in the azimuthal direction. These are shown in figure 5.3.

Secondly, we can note the effect of an off–centred, round aperture on a vortex beam. From the intensity profile seen in figure 5.4, we can note that the doughnut intensity profile has been deformed and does not evenly encircle the vortex core. This could be of experimental use in diagnosing misaligned apertures. A very interesting effect of the off–centred aperture can be seen in the far–field phase map of figure 5.4. The input $l = 3$ beam has been split instead to form three points of vorticity, each with $l = 1$. This is important to note as experimental aperture misalignments may cause this vortex splitting, which would change the interaction behaviour of the beam with experimental samples.

This vortex splitting behaviour also arises when a triangular aperture is used. Similarly to the observed optical case of Mourka *et al.*, the far–field intensity profile of an

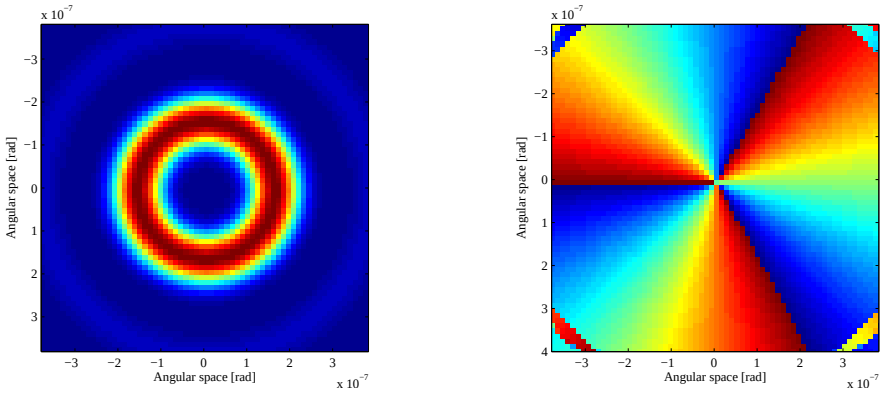

(a) Far–field intensity (b) Far–field phase map

Figure 5.3: Far–field information of a centred, round aperture

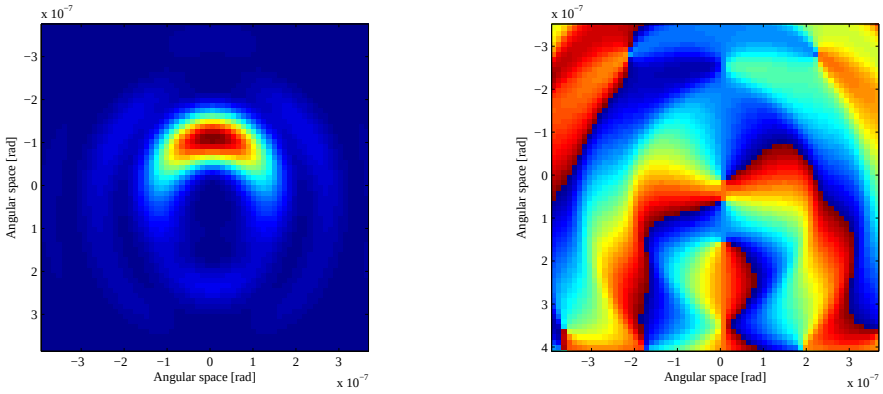

(a) Far–field intensity (b) Far–field phase map

Figure 5.4: Far–field information of an off–centred, round aperture

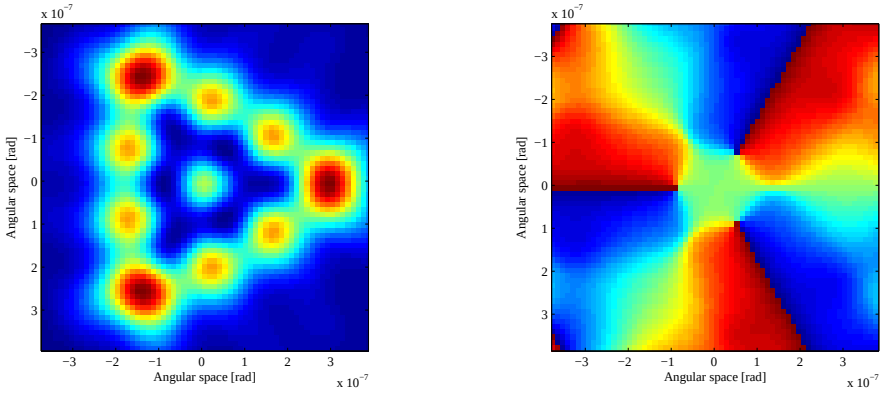

(a) Far–field intensity (b) Far–field phase map

Figure 5.5: Far–field information of a triangular aperture

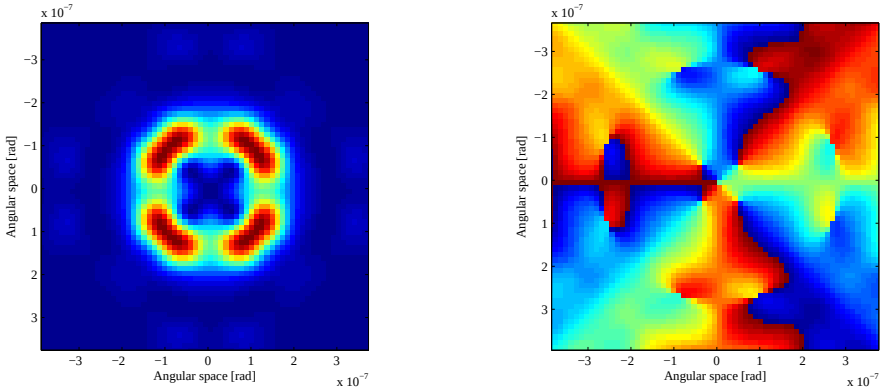

(a) Far–field intensity (b) Far–field phase map

Figure 5.6: Far–field information of a square aperture

electron vortex beam passing through a triangular aperture will produce a triangular array of intensity peaks [69]. This is shown in figure 5.5, and the number of peaks in the intensity pattern is known to be related to the order of OAM of the input beam, enabling application of triangular apertures as a vorticity–measurement tool [69]. Studying the phase map of figure 5.5, we can note that the input $l = 3$ vortex has again split into three $l = 1$ vortices, here arranged in a triangular pattern. This suggests that triangular apertures could also be applied to produce arrays with large numbers of low order vortices. Arrays of low order vortices have found use in optical vortices in trapping experiments [72].

The final case studied in this work, was to apply a square aperture across an $l = 3$ vortex beam. In the far–field intensity profile (seen in figure 5.6), we note an approximately square shaped ring, with a structured region within the centre of the intensity ring. This central region can be understood more clearly by studying the far–field phase map (figure 5.6b.). In this we can note that the input $l = 3$ beam has resulted in four $l = 1$ beams, and one $l = -1$ vortex beam. A vortex–antivortex pair has nucleated such that globally the OAM of the system is conserved.

These apertures have suggested that a high–order vortex state can easily be decom-

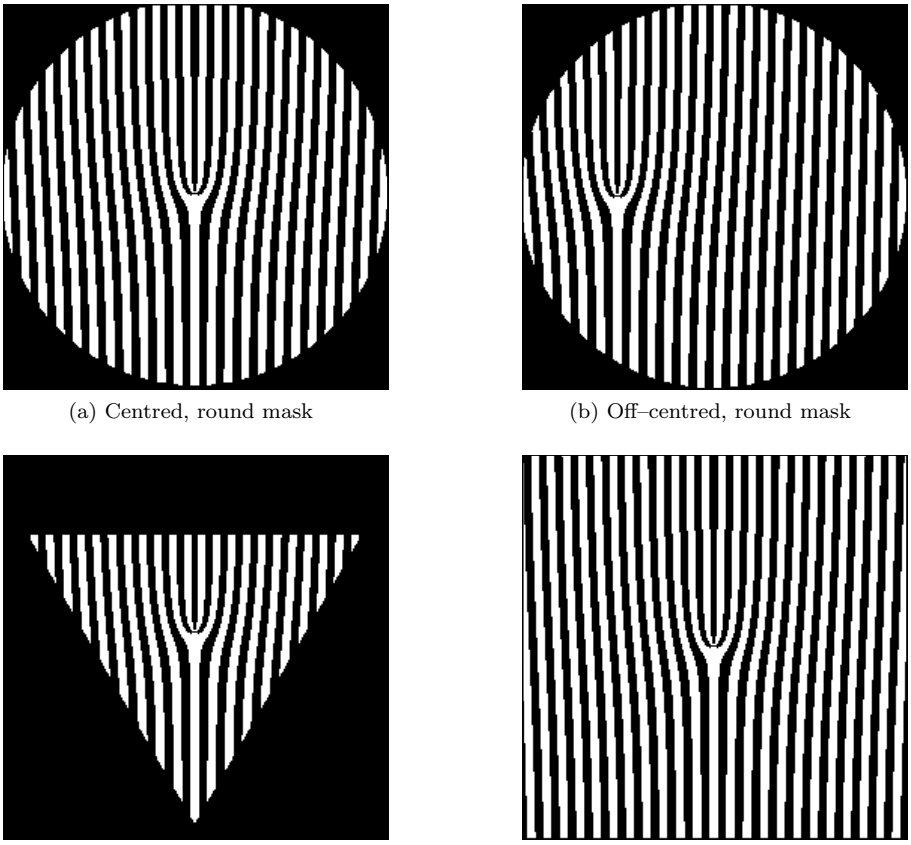

(a) Centred, round mask

(b) Off–centred, round mask

(c) Centred, triangular mask

(d) Centred, square mask

Figure 5.7: Holographic masks resulting from applied aperture shapes

posed into a sum of $|l| = 1$ vortices, forming an array of vortex cores in an arrangement reflecting the symmetry of the aperture. A possible application of apertures, such as those described here, is to analyse beams in order to measure their vorticity, l, via conventional intensity–sensitive detectors.

Alternatively, similar apertures could be incorporated into holographic masks in order to produce many sets of vortex–split sidebeams. This idea is discussed in the following section.

5.3 Aperturing holographic mask

5.3.1 Holgraphic masks

The results shown throughout section 5.2 are of great potential experimental use, however, the method described above would be very difficult to employ in practice. We produce here a method to combine the holographic mask with the geometric apertures and show that this can still create the $|l| = 1$ vortex arrays with one aperture needed in the microscope.

Applying the same phase structures and aperture shapes as shown in figures 5.1 and 5.2 in the holographic mask production process results in the structures shown in figure 5.7. Subfigure 5.7a is the typical $l = 3$ mask, wherein the number of tines of the fork

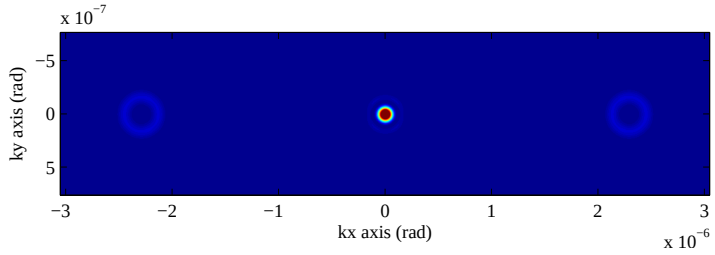

(a) Far–field intensity

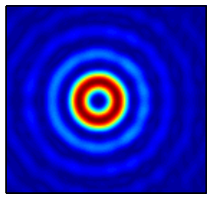

(b) Focus on side beam of centred, round mask

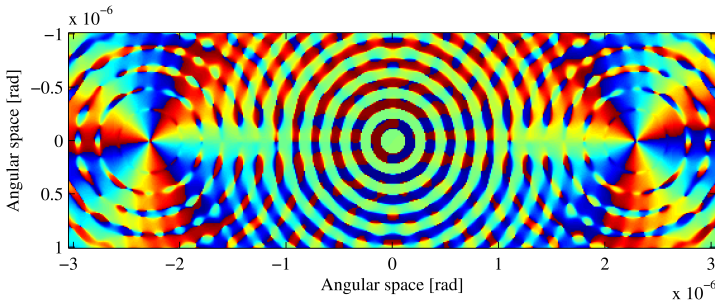

(c) Far–field phase map

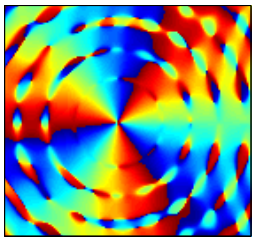

(d) Focus on side beam of centred, round mask

Figure 5.8: Far–field studies of centred, round holographic mask

relates to the order of the first sidebeam as $l + 1$ prongs. The off–centred aperture as seen in subfigure 5.7b is seen to move the position of the fork within the aperture to the equivalent point of the centre of the vortex phase feature. Figures 5.7c and 5.7d are simple combinations of their respective apertures across the expected $l = 3$ fork pattern. The theoretical results from illuminating these masks with an electron beam within a typical TEM are discussed in the following sections.

5.3.2 Far–field results

To understand the effects of these apertures when applied to holographic masks, we discuss the far–field intensity and phase maps of each holographic mask in turn.

The first mask reproduces the simplest results, as considered in chapter 3 of this dissertation. Figure 5.8 displays both the theoretical far–field intensity and phase maps of the centred, round holographic mask. Additionally in figure 5.8b, is a rescaled image of the first–order sidebeam of the far–field results, we note the very strong correlation with figure 5.3. This is as expected, but confirms that the binarisation process is not causing additional effects. The associated phase maps are shown in figure 5.8c and 5.8d, displaying smooth azimuthal phase variation around the vortex centres.

The holographic mask produced from the off–centred vortex term results in the far–field intensity and phase maps displayed in figure 5.9. In this, we can note significant asymmetry between the left– and right–handed sidebeams. This represents a method through which the handedness of the vortex beams can be determined through their intensity patterns alone. The phase maps show the $|l| = 3$ first–ordered sidebeams have split into sets of $|l| = 1$ vortices perpendicularly to the spread of the sidebeams. Further

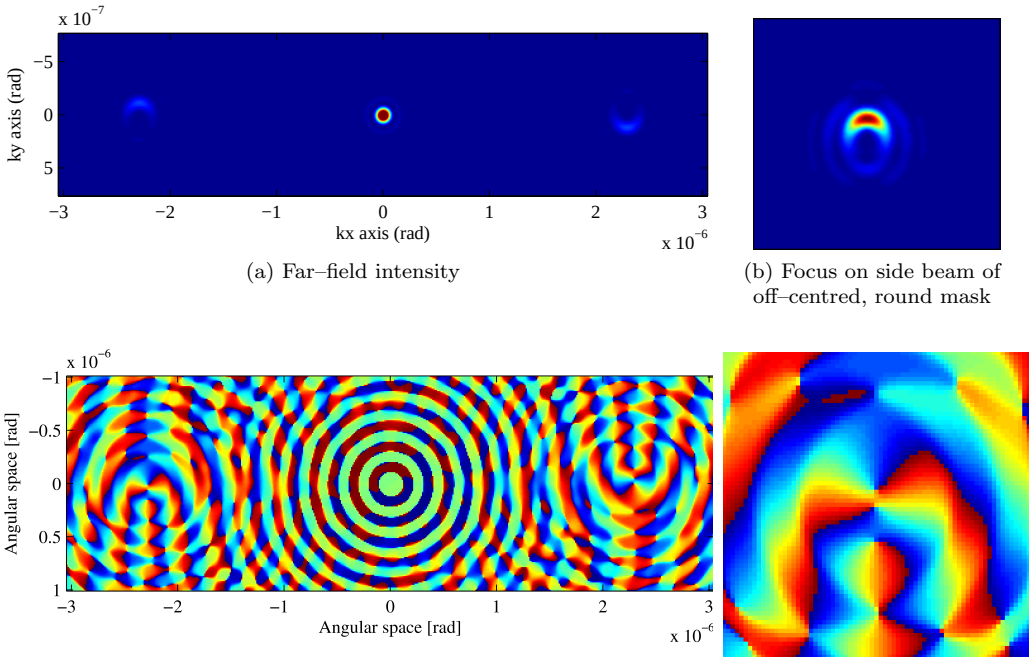

(a) Far–field intensity

(b) Focus on side beam of off–centred, round mask

(c) Far–field phase map

(d) Focus on side beam of off–centred, round mask

Figure 5.9: Far–field studies of off–centred, round holographic mask

study of off centred apertures would be of use to quantify the amound of vortex splitting and whether this spacing can be of use experimentally.

Figure 5.10 shows the far–field intensity and phase maps produced from the triangular holographic mask. The production of many $l = 1$ vortices could be ideal for nanoparticle manipulation and trapping, similarly to the use of optical vortices [65].

The square holographic mask produces the far–field intensity and phase maps shown in figure 5.11. These confirm the vortex splitting and the highly interesting appearance of a vortex–antivortex pair within the first–order sidebeam. The square mask results in a unique arrangement of positive and negative vortices in an array, closely spaced within one sidebeam structure. This may be useful in complex manipulation experiments.

5.4 Summary of aperture shape investigations

The study in this chapter investigated how the shape of the aperture could affect the production of the vortex beams in the far field. Round, triangular and square apertures were applied both across an $l = 3$ phase vortex, and used in the design of the equivalent holographic masks. The round aperture was studied for both a centred and an off–centred design.

The study of the effect of aperture shapes over the vortex beam showed unusual Fraunhofer intensity patterns, quite distinct from their $l = 0$ typical diffraction patterns. Other than the round, centred aperture, the other aperture designs were shown to cause a splitting of the vortex into multiple lower–order vortices. Additional vortices were spontaneously created in $\pm$ pairs, such that topological charge and aperture symmetries were both conserved.

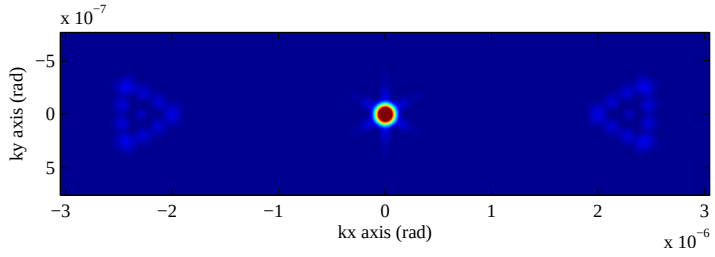

(a) Far–field intensity

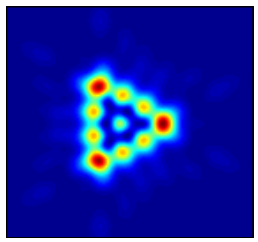

(b) Focus on side beam of triangular mask

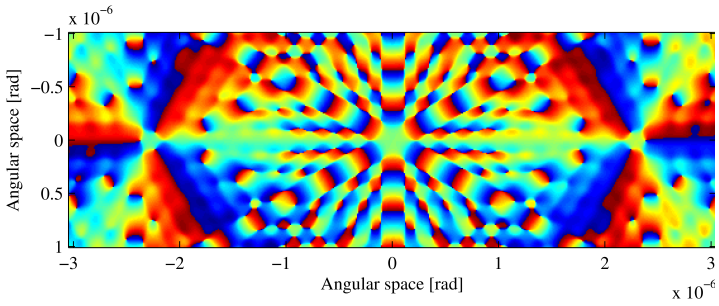

(c) Far–field phase map

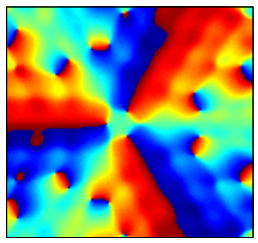

(d) Focus on side beam of triangle mask

Figure 5.10: Far–field studies of triangular holographic mask

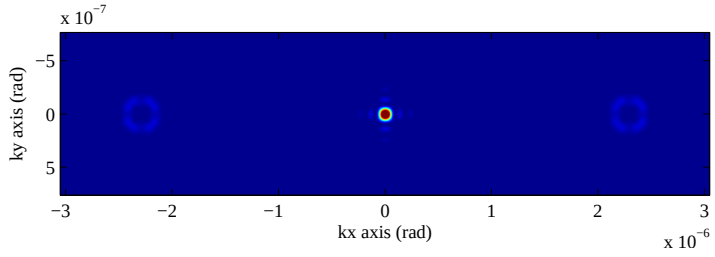

(a) Far–field intensity

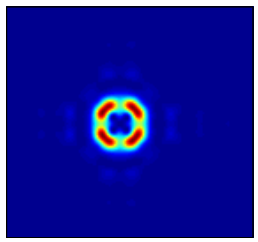

(b) Focus on side beam of square mask

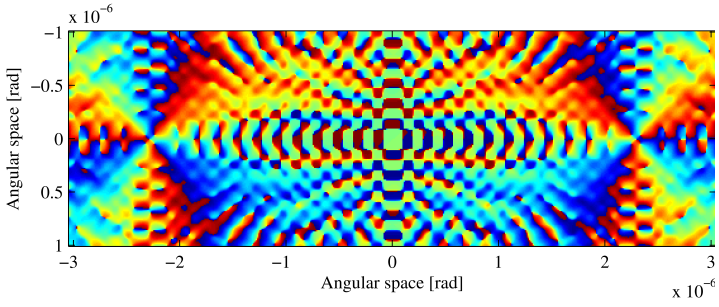

(c) Far–field phase map

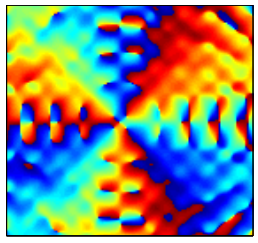

(d) Focus on side beam of square mask

Figure 5.11: Far–field studies of square holographic mask

These features were all found to also appear when the apertures were used in the holographic mask method, which is amenable to experiment.

The creation of small arrays of $l = \pm 1$ electron vortices is expected to be experimentally realisable from these simulations, and the creation of such arrays could prove to be a useful technique for experimental manipulation.

There are two obvious areas of experimental application for this study. Using a triangular aperture at a plane below the holographic mask in the electron microscope column enables a simple quantification of the order of OAM of a vortex beam in an experimentally viable method.

Producing holographic masks with non–cylindrically symmetric apertures can be used for the production of arrays of low order vortex beams, echoing applications of optical vortex beams in particle manipulation. This research also suggests that any imperfect aperture will result in vortex decomposition to lower orders, but if the vortices remain close together, this will be a difficult process to note experimentally as the total order of OAM is conserved, and the splitting occurs within areas of low intensity.

Chapter 6

Conclusions

6.1 Summary remarks

In conclusion, a method has been developed through which holographic masks can be designed to produce vortex beams within an electron microscope. The effects of a number of parameters have been investigated to enable optimisation of spacing and relative intensities for a variety of experimental situations.

In addition to this, the near–field and far–field regimes of these holographic masks have been studied and the effects of a variety of apertures have been investigated.

It is predicted that, similarly to the optical case presented by Mourka *et al.* [69], geometrical apertures can be applied across a vortex beam and the resultant intensity profile can be used to determine the order of vorticity of the beams. This is expected to be simple to implement and to give clear results to determine the order of the vortex beam.

6.2 Future directions and developments

In such a newly developing field as electron vortex beams, there are many as–yet unanswered questions with interest for both theoretical studies and experimental usage. The primary questions developed by this dissertation are to investigate methods of mask production and how their accuracy in reproducing the theoretical design can be improved. Improvements in mask production methods would enable the set of beams in the far–field to be designed with much greater control.

To enable a quantitative study to compare the defocus series', the defocus step–size of the microscope needs to be determined. If this were available, many more properties of electron vortex beams would be accessible to analysis, such as accurate beam divergence studies to enable consideration of the torques and forces involved in electron vortex–nanoparticle manipulation experiments.

It would be highly interesting to experimentally verify the predictions of chapter 5, as this holds potential for both measurement of vortex beams, and production of novel arrays of electron vortex beams, potentially useful for simultaneous manipulation of many particles, or to effect a rotational torque over a larger area of sample than is currently achieveable.

Inclusion of aberrations and limited coherence in the code would allow an increase in accuracy between theoretical predictions and experimental results. This would allow a way to compare the effects of different electron microscope systems on the set of vortex beams they are able to produce. To develop the theoretical accuracy, the code could also be developed to consider electron spin, or electron–electron interactions. This could be achieved by combining the code used here, into a commercially available electron microscopy simulation, such as those discussed by Kirkland [59].

References

[1] Free Digital Photos. `http://www.freedigitalphotos.net`, August 2012.

[2] Sophia Lloyd. Personal Communication, 2012.

[3] Konstantin Bliokh, Yury Bliokh, Sergey Savelev, and Franco Nori. Semiclassical Dynamics of Electron Wave Packet States with Phase Vortices. *Phys. Rev. Lett.*, 99(19):190404, 2007.

[4] Sophia Lloyd, Mohamed Babiker, and Jun Yuan. Quantized Orbital Angular Momentum Transfer and Magnetic Dichroism in the Interaction of Electron Vortices with Matter. *Phys. Rev. Lett.*, 108(7):1, 2012.

[5] Benjamin J. McMorran, Amit Agrawal, Ian M. Anderson, Andrew A. Herzing, Henri J. Lezec, Jabez J. McClelland, and John Unguris. Electron vortex beams with high quanta of orbital angular momentum. *Science*, 331(6014):192, 2011.

[6] J. Verbeeck, H. Tian, and P. Schattschneider. Production and application of electron vortex beams. *Nature*, 467(7313):301, 2010.

[7] A. O'Neil, I. MacVicar, L. Allen, and M. Padgett. Intrinsic and Extrinsic Nature of the Orbital Angular Momentum of a Light Beam. *Phys. Rev. Lett.*, 88(5):5, 2002.

[8] John D. Jackson. *Classical Electrodynamics Third Edition*. Wiley, third edition, August 1998.

[9] J. H. Poynting. The wave motion of a revolving shaft and a suggestion as to the angular momentum in a beam of circularly polarised light. *Proc. Roy. Soc. London A*, 82:560, 1909.

[10] L. Allen, S. M. Barnett, and M. J. Padgett. *Optical Angular Momentum*. Institute of Physics Publishing, 2003.

[11] R. A. Beth. Mechanical Detection and Measurement of the Angular Momentum of Light. *Phys. Rev.*, 50:115, 1936.

[12] J. M. Vaughan and D. V. Willetts. Temporal and interference fringe analysis of TEM_{01}^{*} laser modes. *J. Opt. Soc. Am.*, 73(8):1018, 1983.

[13] Anthony E. Siegman. *Lasers*. University Science Books, 1986.

[14] L. Allen, M. Beijersbergen, R. Spreeuw, and J. Woerdman. Orbital angular momentum of light and the transformation of Laguerre-Gaussian laser modes. *Phys. Rev. A*, 45(11):8185, 1992.

[15] A. Ashkin. Acceleration and trapping of particles by radiation pressure. *Phys. Rev. Lett.*, 24(4):156, 1970.

[16] A. Ashkin, J. M. Dziedzic, J. E. Bjorkholm, and Steven Chu. Observation of a single-beam gradient force optical trap for dielectric particles. *Opt. Lett.*, 11(5):288, 1986.

[17] Deborah Leckband and Jacob Israelachvili. Intermolecular forces in biology. *Quarterly Reviews of Biophysics*, 34:105, 2001.

[18] J. R. Moffitt, R. Yann, Steven B. Smith, and Carlos Bustamante. Recent advances in optical tweezers. *Annual Review of Biochemistry*, 77:205, 2008.

[19] H. He, M. E. J. Friese, N. R. Heckenberg, and H. Rubinsztein-Dunlop. Direct observation of transfer of angular momentum to absorptive particles from a laser beam with a phase singularity. *Phys. Rev. Lett.*, 75(5):826, 1995.

[20] S. J. van Enk and G. Nienhuis. Eigenfunction description of laser beams and orbital angular momentum of light. *Opt. Commun.*, 94:147, 1992.

[21] Mark P. Dennis, Robert P. King, Barry Jack, and Kevin O'Holleran. Isolated optical vortex knots. *Nat. Phys.*, 6:118, 2010.

[22] M. Babiker, C. R. Bennett, D. L. Andrews, and L. C. Dávila Romero. Orbital angular momentum exchange in the interaction of twisted light with molecules. *Phys. Rev. Lett.*, 89:143601, 2002.

[23] S. Franke-Arnold, J. Leach, M. J. Padgett, V. E. Lembessis, D. Ellinas, A. J. Wright, J. M. Girkin, P. Öhberg, and A. S. Arnold. Optical ferris wheel for ultracold atoms. *Opt. Express*, 15(14):8619, 2007.

[24] L. C. Dávila Romero, D. L. Andrews, and M. Babiker. A quantum electrodynamics framework for the nonlinear optics of twisted beams. *J. Optics B-Quantum Semiclassical Optics*, 4:S66, 2002.

[25] Jonathan Leach, Mark R. Dennis, Johannes Courtial, and Miles J. Padgett. Laser beams: Knotted threads of darkness. *Nature*, 432:165, 2004.

[26] L. Allen, M. J. Padgett, and M. Babiker. The orbital angular momentum of light. *Prog. Opt.*, 39:291, 1999.

[27] L. Allen. Introduction to the atoms and angular momentum of light special issue. *Journal of Optics B: Quantum and Semiclassical Optics*, 4(2):S1, 2002.

[28] D. L. Andrews and M. Babiker. *The Angular Momentum of Light*. CUP, 2012.

[29] S. Franke-Arnold, L. Allen, and M. Padgett. Advances in optical angular momentum. *Laser and Photonics Reviews*, 2(4):299, 2008.

[30] J. F. Nye and M. V. Berry. Dislocations in Wave Trains. *Proc. Roy. Soc. London. A*, 336(1605):165, 1974.

[31] Masaya Uchida and Akira Tonomura. Generation of electron beams carrying orbital angular momentum. *Nature*, 464:737, 2010.

[32] Duncan A. Robertson, Peter B. May, and Jim C. G. Lesurf. An omnidirectional circularly polarised antenna. `http://www.st-andrews.ac.uk/~jcgl/Scots_Guide/MMWave/QO/antennas/page1.html`, August 2012.

[33] M. W. Beijersbergen, R. P. C. Coerwinkel, and M. Kristensen. Helical-wavefront laser beams produced with a spiral phaseplate. *Opt. Comm.*, 112:321, 1994.

[34] P. Schattschneider. Theory of free electron vortices. *Ultramicroscopy*, 111:1461, 2011.

[35] Zeinab Mohammadi, Cole P. Van Vlack, Stephen Hughes, Jens Bornemann, and Reuven Gordon. Vortex electron energy loss spectroscopy for near-field mapping of magnetic plasmons. *Opt. Express*, 20(14):15024, 2012.

[36] Koh Saitoh, Yuya Hasegawa, Nobuo Tanaka, and Masaya Uchida. Production of electron vortex beams carrying large orbital angular momentum using spiral zone plates. *Journal of Electron Microscopy*, 61(3):171, 2012.

[37] Juan C. Idrobo and Stephen J. Pennycook. Vortex beams for atomic resolution dichroism. *Journal of electron microscopy*, 60:295, 2011.

[38] J. Verbeeck, P. Schattschneider, S. Lazar, M. Stöger-Pollach, S. Löffler, A. Steiger-Thirsfeld, and G. Van Tendeloo. Atomic scale electron vortices for nanoresearch. *Applied Physics Letters*, 99(20):203109, 2011.

[39] J. Verbeeck, H. Tian, and A. Béché. A new way of producing electron vortex probes for STEM. *Ultramicroscopy*, pages 1–5, 2011.

[40] Konstantin Bliokh, Mark Dennis, and Franco Nori. Relativistic Electron Vortex Beams: Angular Momentum and Spin-Orbit Interaction. *Phys. Rev. Lett.*, 107(17):174802, 2011.

[41] Stefan Löffler and Peter Schattschneider. Elastic propagation of fast electron vortices through crystals. *Acta Crystallographica Section A*, 68(4):443–447, 2012.

[42] Igor P. Ivanov. Colliding particles carrying nonzero orbital angular momentum. *Phys. Rev. D*, 83:093001, 2011.

[43] Igor P. Ivanov. Measuring the phase of the scattering amplitude with vortex beams. *Phys. Rev. D*, 85:076001, Apr 2012.

[44] Igor P. Ivanov. Creation of two vortex-entangled beams in a vortex-beam collision with a plane wave. *Phys. Rev. A*, 85:033813, 2012.

[45] David Bernard Williams and C. Barry Carter. *Transmission Electron Microscopy.* Springer, 1996.

[46] Dr Thirunavukkarasu Gnanavel. Personal Communication, 2012.

[47] S. Chávez-Cerda, M. J. Padgett, I. Allison, G. H. C. New, J. C. Gutiérrez-Vega, A T ONeil, I MacVicar, and J Courtial. Holographic generation and orbital angular momentum of high-order Mathieu beams. *Journal of Optics B: Quantum and Semiclassical Optics*, 4(2):S52, 2002.

[48] D. McGloin and K. Dholakia. Bessel beams: Diffraction in a new light. *Contemporary Physics*, 46:15, 2005.

[49] J. Durnin, J. J. Miceli Jr, and J. H. Eberly. Diffraction-free beams. *Phys. Rev. Lett.*, 58(15):1499, 1987.

[50] H. He, N. R. Heckenberg, and H. Rubinsztein-Dunlop. Optical Particle Trapping with Higher-order Doughnut Beams Produced Using High Efficiency Computer Generated Holograms. *Journal of Modern Optics*, 42(1):217, 1995.

[51] F. Gori and G. Guattari. Bessel–Gauss beams. *Opt. Comm.*, 64(6):491, 1987.

[52] Bahaa E. A. Saleh and Malvin Carl Teich. *Fundamentals of Photonics*. Wiley–Interscience, 2007.

[53] S. M. Lloyd, M. Babiker, and J. Yuan. Interaction of electron vortices and optical vortices with matter and processes of orbital angular momentum exchange. *Phys. Rev. A*, 86:023816, 2012.

[54] Joseph W. Goodman. *Fourier optics*. Roberts and Company, 2005.

[55] Dennis Gabor. A new microscopic principle. *Nature*, 161:777, 1949.

[56] E. N. Leith and J. Upatnieks. Reconstructed wavefronts and communication theory. *J. Opt. Soc. Am.*, 52:1123, 1962.

[57] Akira Tonomura. Development of electron holography and its applications to fundamental problems in physics. *Japanese Journal of Applied Physics*, 47(1):11–18, 2008.

[58] N. R. Heckenberg, R. McDuff, C. P. Smith, H. Rubinsztein-Dunlop, and M. J. Wegener. Laser beams with phase singularities. *Optical and Quantum Electronics*, 24(9):S951–S962, 1992.

[59] Earl J. Kirkland. *Advanced Computing in Electron Microscopy*. Springer, 2010.

[60] Max Born and Emil Wolf. *Principles of Optics*. CUP, 1999.

[61] Dr Jo Verbeeck. Personal Communication, 2012.

[62] Prof. John Rodenburg. `http://www.rodenburg.org`, August 2012.

[63] L. Clark, S. Lloyd, M. Babiker, and J. Yuan. Electron beams with a twist. *Journal of Physics: Conference Series*, 371(1):012005, 2012.

[64] L. Clark. Electron beams with a twist. B.Sc. dissertation, July 2011.

[65] David G. Grier. A revolution in optical manipulation. *Nature*, 424:810, 2003.

[66] David C. Joy. *Monte Carlo Modeling for Electron Microscopy and Microanalysis.* OUP, 2010.

[67] J. M. Cowley and A. F. Moodie. The scattering of electrons by atoms and crystals. I. A new theoretical approach. *Acta Cryst.*, 10:609, 1957.

[68] M. V. Berry and M. R. Dennis. Reconnections of wave vortex lines. *Eur. J. Phys.*, 33:723, 2012.

[69] A. Mourka, J. Baumgartl, C. Shanor, K. Dholakia, and E. M. Wright. Visualization of the birth of an optical vortex using diffraction from a triangular aperture. *Opt. Express*, 19(7):5760, 2011.

[70] J. M. Hickmann, E. J. S. Fonseca, W. C. Soares, and S. Chávez-Cerda. Unveiling a truncated optical lattice associated with a triangular aperture using light's orbital angular momentum. *Phys. Rev. Lett.*, 105:053904, 2010.

[71] Cheng-Shan Guo, Lei-Lei Lu, and Hui-Tian Wang. Characterizing topological charge of optical vortices by using an annular aperture. *Opt. Lett.*, 34(23):3686–3688, 2009.

[72] Jennifer E. Curtis, Brian A. Koss, and David G. Grier. Dynamic holographic optical tweezers. *Optics Communications*, 207(16):169, 2002.